The Astrophysical Journal, 1002:98 (15pp), 2026 May 1 https://doi.org/10.3847/1538-4357/ae5b6f

Temporal Variation in the Coronal Radius Parameter in a Jetted Tidal Disruption Event: Swift J1644+57

Arka Chatterjee[1,2], Kimitake Hayasaki[3,4], Prantik Nandi[5,6], Neeraj Kumari[7,8], Skye R. Heiland[9], Arghajit Jana[10], Sachindra Naik[5], and Samar Safi-Harb[2]

[1] Department of Physics, School of Advanced Engineering, UPES, Dehradun, 248007, India; arka.chatterjee@ddn.upes.ac.in, arka019icsp@gmail.com
[2] Department of Physics & Astronomy, Faculty of Science, University of Manitoba, Winnipeg, Manitoba, R3T 2N2, Canada
[3] Department of Astronomy and Space Science, Chungbuk National University, Cheongju, 361-763, Republic of Korea
[4] Department of Physical Sciences, Aoyama Gakuin University, Sagamihara 252-5258, Japan
[5] Physical Research Laboratory, Navrangpura, Ahmedabad, 380009, India
[6] Indian Centre for Space Physics, Barakhola, Netai Nagar, Kolkata, 700099, India
[7] Indian Institute of Astrophysics, Koramangala, Bengaluru 560 034, India
[8] INAF-IASF Palermo, Via Ugo La Malfa 153, I-90146 Palermo, Italy
[9] Department of Physics & Astronomy, University of British Columbia, Vancouver, BC, V6T 1Z4, Canada
[10] Department of Physics, SRM University-AP, Amaravati, Andhra Pradesh 522240, India
Received 2024 December 19; revised 2026 March 30; accepted 2026 April 1; published 2026 April 28

Abstract

Tidal disruption events are exotic astrophysical phenomena where matter from a star or the interstellar medium is captured by a supermassive black hole. The process liberates enormous energy, within a few months to a year timescale, enough to detect dormant black holes in near as well as the farthest galaxies. We revisit the long-term spectral variabilities associated with the jetted tidal disruption event Swift J1644+57 by exploring the archival X-ray data obtained with the Swift X-ray Telescope and the XMM-Newton observatory. Our analysis reveals that the spectral indices decrease nonmonotonically as Swift J1644+57 evolves with time. We also find that the soft (0.3–1.5 keV) and hard (1.5–10 keV) X-ray photon counts are highly correlated with a maximum correlation coefficient of 0.95 and peak at *zero* lag. Moreover, the soft and hard band variabilities obtained from XMM-Newton observations are highly correlated with a Pearson cross-correlation coefficient of 0.96. This indicates that the soft and hard X-ray photons are emitted from the same site, which is most likely a Compton cloud, i.e., the corona. Assuming the hard X-ray photons originate from the corona, we find that the coronal parameter undergoes rapid expansion during the early phases when accompanied by a relativistic jet launching and subsequently evolves toward a state of saturation with minor fluctuations in the latter stages. The temporal variation in the coronal radius parameter ($R_{\rm cor}$) is consistent with a simple theoretical conjecture. We also discuss the application of our analytical outcomes to other jetted and nonjetted tidal disruption events.

Unified Astronomy Thesaurus concepts: Tidal disruption (1696); Black hole physics (159); Accretion (14); Radiative processes (2055)

1. Introduction

Most galaxies are thought to harbor supermassive black holes (SMBHs) within the mass range of $10^6\,M_\odot \lesssim M_{\rm bh} \lesssim 10^{10}\,M_\odot$ (J. Kormendy & D. Richstone 1995; J. Kormendy & L. C. Ho 2013). The mass of the SMBH has been estimated using the reverberation mapping technique (B. M. Peterson et al. 2004), measuring the proper motion of stars orbiting around the SMBH, and the $M-\sigma_*$ relation, where the velocity dispersion of stars (σ_*) around the galactic bulge is correlated with the mass of the SMBH (M).

Tidal disruption events (TDEs) can provide a unique way to probe the dormant SMBHs in inactive galaxies. A star is tidally disrupted when it reaches within the tidal disruption radius $R_{\rm t} = (M_{\rm bh}/m_*)r_*$, where $M_{\rm bh}$ is the mass of the SMBH, m_* is the stellar mass, and r_* is the stellar radius.

The tidal disruption radius is expressed by

$$\frac{R_{\rm t}}{r_{\rm g}} \approx 50 \left(\frac{M_{\rm bh}}{10^6\,M_\odot}\right)^{-2/3} \times \left(\frac{m_*}{M_\odot}\right)^{-1/3} \left(\frac{r_*}{R_\odot}\right) \quad (1)$$

in units of the gravitational radius, $r_{\rm g} = GM_{\rm bh}/c^2$, where G is the gravitational constant, $M_{\rm bh}$ is the mass of the black hole, and c is the speed of light.

After tidal disruption of the star, the stellar debris falls toward the SMBH and releases its gravitational energy as radiation, generating a luminosity large enough to be comparable to the Eddington limit. According to the standard TDE theory (M. J. Rees 1988; see also E. M. Rossi et al. 2021 for a review), the resultant luminosity decays with time, following the power law of time $t^{-5/3}$, for a span of a few 100 days over the wide range of optical/UV to X-ray wave bands. It is a key observational feature that the light curve decays with $t^{-5/3}$. Though a significant number of TDEs can deviate from the standard $t^{-5/3}$ decay rate due to stellar internal structure (G. Lodato & E. M. Rossi 2011), orbital

eccentricity (K. Hayasaki et al. 2013, 2016, 2018; G. Park & K. Hayasaki 2020; S. Zhong et al. 2023), and/or the penetration factor, which is the ratio of the tidal disruption to pericenter radii (J. Guillochon & E. Ramirez-Ruiz 2013).

The first observational evidence of TDEs dates back to the 1990s (N. Bade et al. 1996) by the All-Sky Survey of the ROSAT satellite. Since then, through multiwavelength campaigns, ∼100 (S. Gezari 2021) have been discovered in a wide range of wave bands from radio to optical/UV to X-ray bands. While most TDEs have been observed in optical/UV wavelengths, ∼10 TDEs have been detected simultaneously in the UV/optical and soft X-ray wavelengths. In addition to these thermal TDEs without a relativistic jet (so-called nonjetted TDEs), there have been so far four remarkable TDEs that accompany a relativistic jet (jetted TDEs), such as Swift J164449.3+573451 (hereafter, Swift J1644+57) (J. S. Bloom et al. 2011a, 2011b; D. N. Burrows et al. 2011; A. J. Levan et al. 2011), Swift J2058+05 (S. B. Cenko et al. 2012), Swift J1112-8238 (G. C. Brown et al. 2015), and AT2022cmc (I. Andreoni et al. 2022).

The event rate of nonjetted TDEs is estimated to be $1 \times 10^{-5}\,\mathrm{yr}^{-1}$ per galaxy for a typical galaxy (J. Magorrian & S. Tremaine 1999; J. L. Donley et al. 2002; J. Wang & D. Merritt 2004), whereas the event rate of jetted TDEs is estimated to be $0.03\,\mathrm{Gpc}^{-3}\ \mathrm{yr}^{-1}$ (H. Sun et al. 2015; F. De Colle & W. Lu 2020; I. Andreoni et al. 2022). Recent observations indicate that many *changing-look* active galactic nuclei (AGNs) have been associated with TDEs (M. Eracleous et al. 1995; A. Merloni et al. 2015; C. Ricci et al. 2020, 2021; A. Jana et al. 2021). This could also potentially increase the population of TDEs with e-ROSITA (A. Merloni et al. 2012) in the future. These event rates indicate the remarkable scarcity of the jetted TDE population. However, the population of jetted TDEs estimated above indicates a relatively small beaming angle ($\leqslant 1^{\circ}$). Of late, the discovery of off-axis jetted TDEs, such as IGR J12580+0134 in the nucleus of NGC 4845 galaxy (R. Walter et al. 2011) and the subsequent radio emission (W.-H. Lei et al. 2016), suggests that the TDEs, which emit hard X-rays with weak radio emission, can show a global property of X-ray TDEs. Several nonjetted, radio-emitting TDEs have also been detected (K. D. Alexander et al. 2020; Y. Cendes et al. 2021). Moreover, the recently discovered association of astrophysical IceCube neutrinos with three TDE candidates (K. Hayasaki 2021; R. Stein et al. 2021) invoked a new era of multimessenger astronomy of TDEs.

There are differences in X-ray spectral hardness between jetted TDEs and nonjetted TDEs. Nonjetted TDEs often exhibit softer spectra, where photon index $\Gamma > 2.5$ is associated with a thermal component (S. Komossa 2017). Contrary to that, jetted TDEs have much harder spectra with $\Gamma \leqslant 2$. In addition, no clear evidence of a thermal component could be observed from the X-ray spectral energy distribution (V. Mangano et al. 2016; E. Seifina et al. 2017). The domain of jetted TDEs began in 2011 March with the discovery of Swift J1644+57. The origin of high-energy γ-rays is traced back to a galaxy at $z = 0.35$ (A. J. Levan et al. 2011). The peak X-ray luminosity exceeded the Eddington limit with the inferred black hole mass $3 \times 10^{6} M_{\odot}$ (J. S. Bloom et al. 2011b; D. N. Burrows et al. 2011; A. J. Levan et al. 2011). The source was detected in radio (Y. Cendes et al. 2014; E. Berger et al. 2012; B. A. Zauderer et al. 2013), infrared (K. Wiersema et al. 2012), X-rays (R. C. Reis et al. 2012; C. J. Saxton et al. 2012; A. González-Rodríguez et al. 2014; V. Mangano et al. 2016; B. A. Zauderer et al. 2013), and γ-rays (J. S. Bloom et al. 2011b; D. N. Burrows et al. 2011). Unlike X-ray luminosity, which decayed over the next 500 days, the radio luminosity increased (E. Berger et al. 2012; B. A. Zauderer et al. 2013) as the event progressed.

E. Seifina et al. (2017) showed that the spectral hardness of the source evolved from $\Gamma \sim 1.8$ to $\Gamma \sim 1.2$ for the first 200 days since the outburst. However, the variation in the spectral index met sudden fluctuations associated with the dips found in the light curve (V. Mangano et al. 2016). From the X-ray spectral shape, luminosity, and the absence of the thermal component, B. A. Zauderer et al. (2013) asserted that the X-ray photons of Swift J1644+57 could not have originated from the accretion disk. Rather, the origin of the X-rays could be from the internal dissipation within the jet at a large distance ($r \sim 10^{4}-10^{5} r_{\mathrm{g}}$) from the SMBH. Contrary to their idea, W.-H. Lei et al. (2016) suggested the X-ray emission from the off-axis jetted TDE candidate IGR J12580+0134 originates from the disk–corona. Beamed accretion, much like in the case of blazars, could stand out as a possible scenario for the hyper accretion rate. However, in the case of Swift J1644+57, the luminosity kept falling with decreasing X-ray photon index (Γ). This observed correlation between luminosity and Γ opposes the "harder when brighter" (H. Krawczynski et al. 2004; M. Gliozzi et al. 2006; Y. H. Zhang et al. 2006; A. Pandey et al. 2017) nature of the X-ray bright blazars and aligns with the accretion-disk-dominated Seyferts or galactic black holes (GBHs; e.g., Q.-X. Yang et al. 2015; A. Jana 2022; A. Jana et al. 2026). Stronger evidence of the accretion disk origin of the X-ray emission in Swift J1644+57came from E. Kara et al. (2016), where reverberation lag was observed.

A quasiperiodic oscillation (QPO) of 200 s, within the first 20 days from the peak luminosity, was discovered from the X-ray light curves in the 2–10 keV energy band, using the *Suzaku* and XMM-Newton observations (R. C. Reis et al. 2012; C. J. Saxton et al. 2012). Similar QPOs in X-rays have been observed for two other TDE candidates, namely, 2XMM J123103.2+110648 (D. Lin et al. 2013) and ASASSN-14li (D. R. Pasham et al. 2019). M. Nikołajuk & R. Walter (2013) suggested the detection of a QPO within 0.0008-0.004 Hz for IGR J12580+0134, where the timescale is consistent for a TDE with central black hole mass $\sim 10^{5} M_{\odot}$. There are many arguments that the QPOs can bridge the mass gap between the accretion processes of galactic, stellar-mass black holes, and SMBHs (S. Vaughan & P. Uttley 2005). However, very few of them are detected with statistical confidence for AGNs (M. Gierliński et al. 2008; W. N. Alston et al. 2015; D. I. Ashton & M. J. Middleton 2021). There are many challenges for observing QPOs originating from AGNs, apart from achieving a statistically significant signal-to-noise ratio (S. Vaughan & P. Uttley 2006). Considering the mass of Swift J1644+57, the 200 s QPO found in the X-ray light curve requires a scale of $\mathcal{O}(10)\ r_{\mathrm{s}}$ for a nonrotating SMBH. This scale fits within the range of the typical coronal radius parameter (hereafter R_{cor}) of TDEs as proposed by A. Mummery & S. A. Balbus (2021), and is also consistent with the corona size, which is observationally suggested for many AGNs (W. N. Alston et al. 2020). Thus, we expect to find a reasonable explanation of hard X-ray variations through the

disk–corona geometry by analyzing the existing data of jetted TDEs. The most promising mechanism for the luminous emission of TDEs is a thermal blackbody emission. S. Gezari (2021) suggested that there is a bimodal distribution of the TDE thermal emission, indicating that the soft X-ray photons are produced from the inner disk region, whereas the optical/UV photons could be emitted from the photospheric outflows. The thermal photons produced from the disk can be a good candidate source for the Compton scattering. This suggests a disk–corona system can exist in X-ray TDEs.

A. A. Galeev et al. (1979) first proposed the disk–corona system to explain the hard X-ray origin of Galactic X-ray binaries. They formulated it based on an analogy with the solar coronal structure. The corona is heated through the magnetic reconnection at the disk surface and also through the convection within an accretion disk. As the inward flow progresses onto the black hole, the coronal structure can be dynamic, and the magnetic field strength increases, giving rise to a central cloud composed of hot electrons ($\sim 10^8$ K) and a magnetic field strength on the order of 10^7 Gauss. This model can explain the hard X-ray emission from Cyg X-1. F. Haardt & L. Maraschi (1991) proposed a two-phase component model, where the standard accretion disk surrounding the corona emits the soft photons, which are also reprocessed in the corona via Comptonization and reflection. The model was able to explain the general features of AGN spectra. Subsequently, A. Martocchia & G. Matt (1996) and G. Miniutti & A. C. Fabian (2004) proposed the *Lamppost* model, which includes the effect of the gravitational bending due to the black hole spin and the reflection effect by the iron Kα line (A. C. Fabian & I. M. George 1991; Y. Tanaka et al. 1995). Moreover, B. F. Liu et al. (2002) constructed a simple theoretical disk–corona model, where the corona is heated by magnetic reconnection and cooled by Compton scattering. The origin of the very high-temperature corona was considered to be the magnetic field for all of the abovementioned models. More recently, C. Done et al. (2012) provided a more observationally consistent model, *Optxagnf*. This model provides a spectral fit originating from the corona and disk with sub- to super-Eddington accretion flows of AGNs. Their model also provides a practical estimate for the coronal size. In the TDE context, A. Mummery & S. A. Balbus (2021) applied the simple empirical model, where the corona expands as the luminosity decays and the smallest coronal parameter ($R_{\rm cor}$) corresponds to the peak luminosity, to model the hard X-ray profile seen in the six nonjetted TDEs.

In this paper, we study how the Compton cloud of the jetted TDE Swift J1644+57 varies with time by using the *Optxagnf* model and whether the model can explain the hard X-ray properties. The paper is structured in the following way. In Section 2, we explain the data analysis method and the subsequent processing. In Section 3, we describe our results obtained from data analysis. We then discuss our findings and the implications for TDEs in Section 4. Finally, we summarize our conclusions in Section 5.

2. Data Analysis Process

We used the archival data of XMM-Newton and Swift/X-ray Telescope (XRT) obtained through HEASARC.[11] We reprocessed all data using `HEAsoft v6.26.1` (K. A. Arnaud 1996), which includes `XSPEC v12.10.1f`. We use the following cosmological parameters in this work: $H_0 = 70$ km s^{-1} Mpc^{-1}, $\Lambda_0 = 0.73$, $\Omega_M = 0.27$ (C. L. Bennett et al. 2003). With the cosmological parameters, the luminosity distance of Swift J1644+57 was considered 1402.8 Mpc (A. J. Levan et al. 2011).

2.1. Swift/XRT

XRT (D. N. Burrows et al. 2005) on board Swift has the highest cadence monitoring observation of Swift J1644+57 in the X-ray band (0.3 to 10.0 keV), especially during the TDE from 2011. Depending on the brightness of the source, XRT observed this source in both Window Timing (WT) and Photon Counting (PC) modes. The source was observed by Swift/XRT over ~500 times from 2011 March 31 to 2012 September 30. We stacked all observations into 17 segments depending on the brightness of the source. When the event started, the source was brighter. Thus, we stacked ~15 observations into a single spectrum and produced the combined spectrum. This procedure is followed for the first 154 observations. We stacked these observations into 10 combined observations (XRT1 to XRT10) (details are given in Table 1). After that, the source became dimmed with respect to previous observations. For that, we stacked ~40 observations into a single spectrum. This process is followed for the next 250 observations and produces the stacked spectrum from XRT11 to XRT15 (see Table 1). After 2012 March 17, we stacked 176 observations and 108 observations into a combined observation for XRT16 and XRT17, respectively. We use the online tool "XRT product builder"[12] (P. A. Evans et al. 2009) to extract the spectrum and light curves. This product builder performs all necessary processing and calibration and produces the final spectra and light curves of Swift J1644+57 WT and PC modes. The GRPPHA task is used with 10 counts per bin for XRT spectra. For more details, see Table 1.

2.2. XMM-Newton

We reprocessed the XMM-Newton Epic-pn data using the Science Analysis Software (SAS) v17.0.0 and updated calibration files. We reprocessed the data with the "epproc" task. For each observation ID, we created good time interval (GTI) files after eliminating the intervals of flaring particle background based on the count rate in the light curves above 10 keV. We filtered the event lists to get the good events with a pattern $< = 4$ for a given GTI file and generated the cleaned event lists. We extracted source and background spectra using circular regions of radii 30″ and 50″, respectively. We generated the light curves in 0.2–2 keV and 3–10 keV ranges with a 10 s time bin and corrected for effects like vignetting, bad pixels, and variations in the point-spread function. We also checked for any pileup effects in the data. We generated the redistribution matrix and ancillary response files using the SAS tasks "rmfgen" and "afrgen," respectively. We grouped the spectrum with a minimum of 20 counts per bin and oversampled it by a factor of 3 using the "specgroup" task.

[11] http://heasarc.gsfc.nasa.gov/

[12] https://www.swift.ac.uk/user_objects/

Table 1
Observation Log for Swift/XRT and XMM-Newton Observations of Swift J1644+57

ID	Date (yyyy-mm-dd)	Obs. ID	Instrument	Total Exposure (ks)
XRT1	2011-03-31	00031955002	Swift/XRT	224
⋯	−2011-04-14	−00031955016	⋯	⋯
XMM1	2011-03-31	0658400701	XMM-Newton/Epic-pn	26
XRT2	2011-04-15	00031955017	Swift/XRT	210
⋯	−2011-04-30	−00031955032	⋯	⋯
XMM2	2011-04-16	0678380101	XMM-Newton/Epic-pn	25
XMM3	2011-04-30	0678380201	XMM-Newton/Epic-pn	29
XRT3	2011-05-01	00031955033	Swift/XRT	137
⋯	−2011-05-13	−00031955047	⋯	⋯
XRT4	2011-05-14	00031955048	Swift/XRT	162
⋯	−2011-05-29	−00031955063	⋯	⋯
XMM4	2011-05-16	0678380301	XMM-Newton/Epic-pn	30
XRT5	2011-05-30	00031955064	Swift/XRT	125
⋯	−2011-06-12	−00031955078	⋯	⋯
XMM5	2011-05-30	0678380401	XMM-Newton/Epic-pn	30
XRT6	2011-06-13	00031955079	Swift/XRT	131
⋯	−2011-06-26	−00031955093	⋯	⋯
XRT7	2011-06-27	00031955094	Swift/XRT	142
⋯	−2011-07-13	−00031955109	⋯	⋯
XMM6	2011-07-03	0678380501	XMM-Newton/Epic-pn	19
XRT8	2011-07-14	00031955110	Swift/XRT	80
⋯	−2011-07-28	−00031955124	⋯	⋯
XMM7	2011-07-15	0678380601	XMM-Newton/Epic-pn	30
XMM8	2011-07-15	0678380701	XMM-Newton/Epic-pn	19
XRT9	2011-07-29	00031955125	Swift/XRT	77
⋯	−2011-08-12	−00031955139	⋯	⋯
XRT10	2011-08-13	00031955140	Swift/XRT	56
⋯	−2011-08-27	−00031955154	⋯	⋯
XMM9	2011-08-14	0678380801	XMM-Newton/Epic-pn	29
XMM10	2011-08-27	0678380901	XMM-Newton/Epic-pn	30
XRT11	2011-08-28	00031955155	Swift/XRT	108
⋯	−2011-10-01	−00031955190	⋯	⋯
XMM11	2011-09-06	0678381001	XMM-Newton/Epic-pn	28
XMM12	2011-09-06	0678381101	XMM-Newton/Epic-pn	28
XMM13	2011-10-02	0678381201	XMM-Newton/Epic-pn	28
XRT12	2011-10-03	00031955191	Swift/XRT	110
⋯	−2011-11-11	−00031955230	⋯	⋯
XRT13	2011-11-12	00031955231	Swift/XRT	132
⋯	−2011-12-21	−00032200015	⋯	⋯
XRT14	2011-12-22	00032200016	Swift/XRT	104
⋯	−2012-01-30	−00032200055	⋯	⋯
XRT15	2012-01-31	00032200056	Swift/XRT	116
⋯	−2012-03-17	−00032200100	⋯	⋯
XRT16	2012-03-18	00032200101	Swift/XRT	120
⋯	−2012-06-07	−00032200175	⋯	⋯
XRT17	2012-06-08	00032200101	Swift/XRT	156
⋯	−2012-09-30	−00032526046	⋯	⋯

3. Results

3.1. Light Curves

The long-term X-ray light curve obtained from the Swift/XRT showed a high degree of variation during the TDE of Swift J1644+57. The source counts changed dramatically by orders of magnitude (see Figure 1) within the span of ∼600 days. We split the energy band of Swift into 0.3–1.5 keV and 1.5–10.0 keV ranges. As evident from Figures 1 and 2, the hard band dominated the entire episode with sudden dips occasionally observed (V. Mangano et al. 2016).

We performed cross-correlation analysis using the ζ–discrete cross-correlation function (ZDCF;[13] T. Alexander 1997) on the long-term light curve obtained from the Swift/XRT satellite. The ζ–DCF method provides a better estimate of the cross-correlation function for unevenly sampled datasets and considers the nonlinearity while interpolating the lightcures. The cross-correlation study yields an optimal correlation of the 0.3–1.5 and 1.5–10 keV energy bands, having a correlation coefficient $\rho_{\max} = 0.95$. The correlation pattern peaked at a

[13] ZDCF: http://www.weizmann.ac.il/particle/tal/research-activities/software

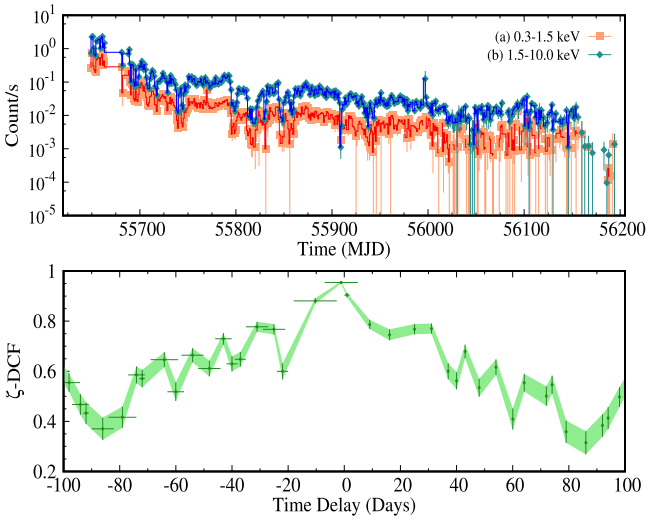

Figure 1. Upper panel: X-ray light curves of Swift J1644+57, obtained from the Swift/XRT, are presented for 0.3–1.5 keV (square, light salmon) and 1.5–10 keV energy bands (diamond, greenish-blue points). Lower panel: The ζ–DCF cross correlation between 0.3–1.5 keV and 1.5–10 keV ranges is presented for Swift J1644+57 using Swift/XRT data. Both the energy bands are highly correlated ($\rho_{max} = 0.95$). Considering the error bars, no delay is observed between the two X-ray bands.

negative delay of 1.09 ± 5.9 days. Considering the measurement error, this could be considered as a zero delay between the two energy bands of the X-ray. A similar zero delay was also observed for an outbursting GBH, named XTE J1550-564, where a relatively smaller size of the accretion disk is attributed to the absence of any delay (A. Chatterjee et al. 2020). The light curve, along with the ZDCF, is presented in Figure 1.

From the light curve of Swift/XRT, we obtained the hardness ratio (HR) as presented in V. Mangano et al. (2016) and E. Seifina et al. (2017). We found that the source counts in the hard band were always greater (see Figure 2) than in the soft band. As the event progressed, the contribution of the hard band in the light curve also increased, making harder spectra at the late time of the TDE. The left panel of Figure 2 shows the 'HR' diagram obtained using the first 90 days of data.

Using XMM-Newton data, we calculated the fractional variability (F_{var}; R. A. Edelson et al. 1996; K. Nandra et al. 1997; R. Edelson et al. 2001; S. Vaughan et al. 2003; R. Edelson & M. Malkan 2012) in the 0.2–2 and 3–10 keV bands. The light curves (presented as x_i counts s^{-1}) contain uncertainties σ_i of length N with a mean μ and standard deviation σ, related by,

$$F_{var} = \sqrt{\frac{\sigma_{XS}^2}{\mu^2}}, \tag{2}$$

where σ_{XS}^2 is the excess variance (K. Nandra et al. 1997; R. Edelson et al. 2002). σ_{XS}^2 is defined as,

$$\sigma_{XS}^2 = \sigma^2 - \sigma_{err}^2, \tag{3}$$

where σ_{err}^2 is the mean squared error. The σ_{err}^2 is given by,

$$\sigma_{err}^2 = \frac{1}{N}\sum_{i=1}^{N}\sigma_i^2. \tag{4}$$

The normalized excess variance is given by,

$$\sigma_{NXS}^2 = \frac{\sigma_{XS}^2}{\mu^2}. \tag{5}$$

The uncertainties in F_{var} and σ_{NXS} (S. Vaughan et al. 2003) are given by,

$$\mathrm{err}(F_{var}) = \sqrt{\left(\sqrt{\frac{1}{2N}}\frac{\sigma_{err}^2}{\mu^2 F_{var}}\right)^2 + \left(\frac{1}{\mu}\sqrt{\frac{\sigma_{err}^2}{N}}\right)^2}, \tag{6}$$

and

$$\mathrm{err}(\sigma_{NXS}^2) = \sqrt{\left(\sqrt{\frac{2}{N}}\frac{\sigma_{err}^2}{\mu^2}\right)^2 + \left(\sqrt{\frac{\sigma_{err}^2}{N}}\frac{2F_{var}}{\mu}\right)^2}. \tag{7}$$

Table 2 presents the results of our variability study in soft and hard bands. The excess variance or σ_{NXS}^2 yielded a negative value, which resulted in an imaginary fractional variability (F_{var}) for the XMM5 observation. The maximum of σ_{NXS}^2 or F_{var} is observed during XMM3. The F_{var} of the hard band is found to be higher than its softer counterpart for all XMM-Newton observations. We find that the F_{var} between 0.2–2 and 3–10 keV, presented in the right panel of Figure 2, is highly correlated with a correlation coefficient of 0.96.

3.2. Spectra

To understand the X-ray spectral properties of Swift J1644+57, we used the phenomenological model along with the physical model. During fitting, we employed stacked XRT spectra to obtain a broad idea of spectral variations. All errors are quoted with 90% confidence level, unless specified otherwise.

We started the spectral fitting with the `powerlaw` model, and the model in `XSPEC` reads as: `TBabs*zTBabs*(powerlaw)`.

The galactic hydrogen column density (N_H) was kept frozen at 0.016×10^{22} cm^{-2} throughout the entire spectral fitting process. The initial fits with the `powerlaw` model provide a good fit with $\chi^2_{red} \sim 1$. Table 3 presents the findings of the fits. During the first observation, which spans from MJD 55651 to MJD 55665, the spectral index of the source was observed to be 1.79 ± 0.02. Corresponding N_H was found to be $1.75 \pm 0.04 \times 10^{22}$ cm^{-2}. The normalization of the `powerlaw` component was observed to be the highest, 0.0177 ± 0.005 ph cm^{-2} s^{-1}, among all other observations. Our second observation was made by stacking Swift/XRT spectra within the duration of MJD 55666 to MJD 55681. The spectrum was fitted with a power-law index $\Gamma = 1.62 \pm 0.01$ and corresponding N_H was found to be $1.44 \pm 0.03 \times 10^{22}$ cm^{-2}. The normalization and flux, presented in Table 3, were found to be decreased compared to the first observation. This is consistent with the light curve. We found the highest reduced chi-square ($\chi^2_{red} \sim 1.21$) for this particular observation. The fitted unfolded spectrum is presented in the left panel of Figure 3. The following observation considered the stacked spectra within MJD 55682 to MJD 55694. The source flux decreased substantially in the XRT3 observation. We found a higher N_H compared to the previous observation. The spectral indices had increased in XRT4 and XRT5 compared to the previous observations, XRT2 and XRT3. Apart from that, the

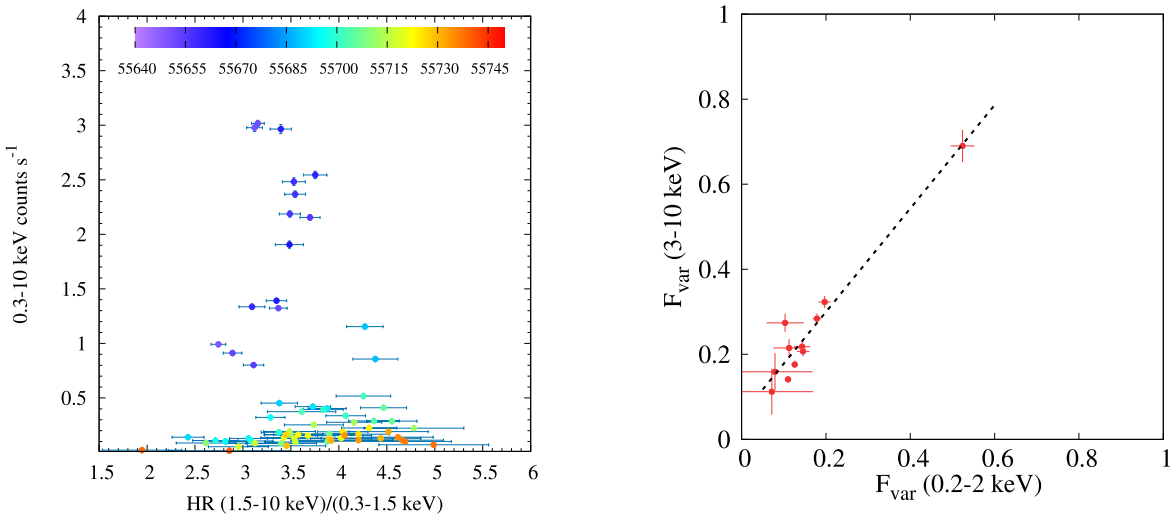

Figure 2. Left panel: The hardness ratio of Swift J1644+57 is presented. The source exhibited hard spectra throughout the TDE. The color bar on top represents the MJD from the start of the event. Right panel: The correlated variability between 0.2–2 and 3–10 keV is observed from XMM-Newton data. The Pearson correlation coefficient is 0.96.

Table 2
Variability Statistics in Various Energy Ranges Are Shown in This Table

ID	Energy Band (keV)	N	$x_{\max}$ (counts s^{-1})	$x_{\min}$ (counts s^{-1})	$\frac{x_{max}}{x_{min}}$	σ^2_{NXS} (10^{-2})	F_{var} (%)
XMM1	0.2–2.0	451	8.34	3.69	2.26	1.21 ± 0.08	11.0 ± 0.51
XMM2	0.2–2.0	378	6.39	1.77	3.56	1.59 ± 0.16	12.6 ± 0.78
XMM3	0.2–2.0	301	1.46	0.02	60.8	27.4 ± 2.45	52.4 ± 2.83
XMM4	0.2–2.0	540	1.72	0.37	4.67	2.92 ± 3.19	17.8 ± 1.04
XMM5	0.2–2.0	302	0.30	0.03	11.8	−0.04 ± 2.95	⋯
XMM6	0.2–2.0	491	1.52	0.18	8.60	3.90 ± 0.50	19.7 ± 1.41
XMM7	0.2–2.0	322	1.01	0.13	8.00	2.06 ± 0.52	14.3 ± 1.92
XMM8	0.2–2.0	544	0.94	0.15	6.16	2.12 ± 0.41	15.6 ± 1.46
XMM9	0.2–2.0	513	0.36	0.03	14.3	0.51 ± 0.14	7.2 ± 9.80
XMM10	0.2–2.0	521	0.49	0.02	20.1	1.27 ± 0.84	11.2 ± 3.75
XMM11	0.2–2.0	386	0.43	0.02	17.3	0.63 ± 1.41	7.9 ± 8.89
XMM12	0.2–2.0	389	0.77	0.04	17.8	1.12 ± 0.91	10.3 ± 4.41
XMM1	3.0–10.0	451	6.57	2.25	2.93	2.01 ± 0.12	14.1 ± 0.63
XMM2	3.0–10.0	378	5.28	3.33	2.92	3.10 ± 0.22	17.6 ± 0.89
XMM3	3.0–10.0	300	1.62	0.02	66.6	44.7 ± 3.53	69.0 ± 3.80
XMM4	3.0–10.0	540	2.04	0.19	10.8	8.15 ± 0.47	28.4 ± 1.20
XMM5	3.0–10.0	299	0.26	0.03	10.1	−0.03 ± 0.03	⋯
XMM6	3.0–10.0	491	2.34	0.20	11.4	10.4 ± 0.63	32.3 ± 1.42
XMM7	3.0–10.0	322	1.36	0.26	5.31	4.81 ± 0.59	21.8 ± 1.60
XMM8	3.0–10.0	544	1.53	0.23	6.54	4.32 ± 0.41	20.7 ± 1.17
XMM9	3.0–10.0	513	0.36	0.03	14.0	1.30 ± 1.21	11.2 ± 5.41
XMM10	3.0–10.0	521	0.68	0.03	27.1	4.61 ± 0.86	21.5 ± 2.10
XMM11	3.0–10.0	389	0.44	0.03	17.3	2.54 ± 1.38	15.9 ± 4.40
XMM12	3.0–10.0	387	0.92	0.05	17.7	7.51 ± 1.05	27.4 ± 2.15

Note. We have opted for 100 s time bins for variability analysis. In some cases, the average error of observational data exceeds the limit of 1σ, resulting in negative excess variance. In such cases, we have imaginary $F_{\rm var}$, which are not shown in the table.

$N_{\rm H}$ had increased, and the corresponding flux decreased. We found a general trend of decreasing Γ up to XRT11. The corresponding $N_{\rm H}$ also increased, and the luminosity exhibited a decreasing pattern. The findings were comparable with the findings of E. Seifina et al. (2017). However, from XRT12, the spectral index started to increase. However, it should be noted that the errors corresponding to the spectral indices became larger as the source became dim and data quality was reduced. For XRT16 observation, we found the source spectrum showed a steeper Γ at 1.72 ± 0.22, comparable to the initial days of the TDEs. The left Panel of Figure 4 shows the 90% confidence contours of $N_{\rm H}$ and Γ. The spectral parameter variations, fitted with the `powerlaw` model, are presented in Figure 5.

Swift J1644+57 was observed by MM-Newton 12 times within the duration of the initial phase of the TDE, ranging from MJD 55667 to MJD 55836. We fitted the XMM-Newton data with the `powerlaw` model to compare the parameter

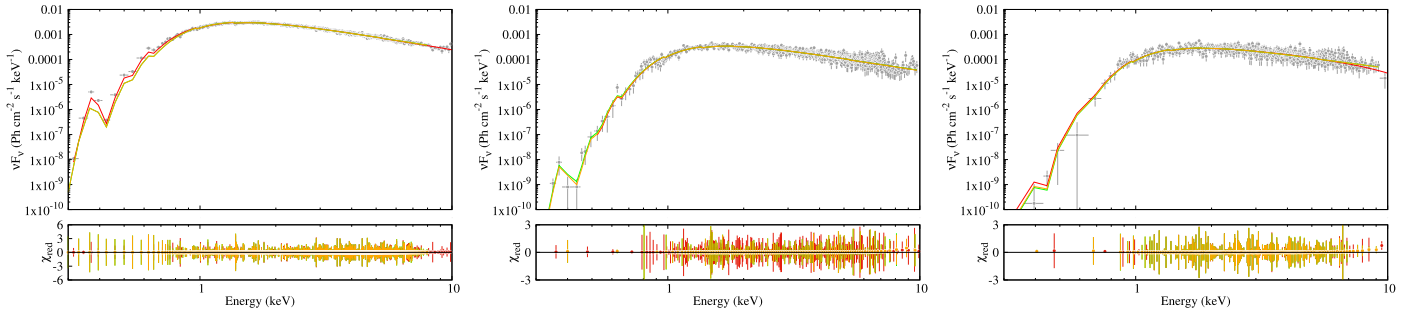

Figure 3. Left to right: XRT2, XRT6, and XRT10 fitted unfolded spectra are presented for various models. The red line represents the `Optxagnf` model, green represents the `Nthcomp` model, and orange represents the `powerlaw` model. Corresponding residues are plotted in the bottom panels.

Table 3
`powerlaw` Fitting Result for the 0.3–10 keV Energy Range

ID	MJD (days)	$N_{\rm H}$ (10^{22} cm^{-2})	Γ	N (10^{-3})	log(Flux) (10^{-11} erg cm^{-2} s^{-1})	χ^2/dof
			Swift/XRT			
XRT1	55658	$1.75^{+0.04}_{-0.04}$	$1.79^{+0.02}_{-0.02}$	$17.7^{+5.50}_{-5.50}$	−09.94	902.74/827
XRT2	55673.5	$1.44^{+0.03}_{-0.03}$	$1.62^{+0.01}_{-0.01}$	$10.8^{+2.12}_{-2.12}$	−10.09	1047.47/861
XRT3	55688	$1.67^{+0.08}_{-0.08}$	$1.63^{+0.04}_{-0.04}$	$4.51^{+2.74}_{-2.74}$	−10.48	741.23/866
XRT4	55702.5	$1.90^{+0.08}_{-0.08}$	$1.75^{+0.04}_{-0.04}$	$3.10^{+1.73}_{-1.73}$	−10.63	525.19/703
XRT5	55717.5	$1.99^{+0.10}_{-0.10}$	$1.74^{+0.05}_{-0.05}$	$2.20^{+1.60}_{-1.60}$	−10.83	574.73/643
XRT6	55731.5	$1.95^{+0.11}_{-0.11}$	$1.61^{+0.05}_{-0.05}$	$1.47^{+1.13}_{-1.13}$	−10.96	615.79/640
XRT7	55747	$2.13^{+0.15}_{-0.15}$	$1.62^{+0.07}_{-0.07}$	$0.96^{+0.96}_{-0.96}$	−11.14	596.64/594
XRT8	55763	$1.89^{+0.13}_{-0.13}$	$1.45^{+0.07}_{-0.07}$	$1.26^{+0.12}_{-0.12}$	−10.96	555.14/596
XRT9	55778	$1.94^{+0.16}_{-0.16}$	$1.56^{+0.07}_{-0.07}$	$1.33^{+0.14}_{-0.14}$	−10.98	508.38/544
XRT10	55793	$2.21^{+0.20}_{-0.20}$	$1.40^{+0.09}_{-0.09}$	$1.12^{+0.15}_{-0.15}$	−10.98	498.03/520
XRT11	55818	$2.04^{+0.22}_{-0.22}$	$1.44^{+0.10}_{-0.10}$	$0.46^{+0.07}_{-0.07}$	−11.39	431.81/475
XRT12	55856.5	$2.14^{+0.19}_{-0.19}$	$1.57^{+0.10}_{-0.10}$	$0.72^{+0.09}_{-0.09}$	−11.25	466.99/509
XRT13	55896.5	$2.15^{+0.19}_{-0.19}$	$1.50^{+0.09}_{-0.09}$	$0.58^{+0.07}_{-0.07}$	−11.31	441.98/519
XRT14	55936	$2.18^{+0.39}_{-0.39}$	$1.61^{+0.16}_{-0.16}$	$0.38^{+0.10}_{-0.10}$	−11.54	274.05/309
XRT15	55980	$1.94^{+0.24}_{-0.24}$	$1.55^{+0.12}_{-0.12}$	$0.32^{+0.06}_{-0.06}$	−11.59	337.79/371
XRT16	56044.5	$2.23^{+0.55}_{-0.55}$	$1.72^{+0.22}_{-0.22}$	$0.21^{+0.08}_{-0.08}$	−11.84	166.80/197
XRT17	56143	$1.76^{+0.80}_{-0.80}$	$1.28^{+0.34}_{-0.34}$	$0.04^{+0.02}_{-0.02}$	−12.40	99.32/104
			XMM-Newton			
XMM1	55667	$1.29^{+0.01}_{-0.01}$	$1.69^{+0.01}_{-0.01}$	$13.56^{+0.10}_{-0.10}$	−10.02	224.69/174
XMM2	55681	$1.42^{+0.02}_{-0.02}$	$1.54^{+0.01}_{-0.01}$	$8.87^{+0.10}_{-0.10}$	−10.15	186.68/173
XMM3	55697	$1.33^{+0.06}_{-0.06}$	$1.87^{+0.05}_{-0.05}$	$1.18^{+0.07}_{-0.08}$	−11.14	141.20/133
XMM4	55711	$1.49^{+0.04}_{-0.03}$	$1.55^{+0.02}_{-0.02}$	$2.48^{+0.07}_{-0.07}$	−10.71	193.00/167
XMM5	55745	$1.41^{+0.14}_{-0.13}$	$1.59^{+0.08}_{-0.08}$	$0.27^{+0.03}_{-0.03}$	−11.68	97.00/90
XMM6	55757	$1.61^{+0.05}_{-0.05}$	$1.39^{+0.02}_{-0.02}$	$1.68^{+0.06}_{-0.06}$	−10.80	186.57/162
XMM7	55769	$1.62^{+0.06}_{-0.06}$	$1.41^{+0.03}_{-0.03}$	$1.44^{+0.07}_{-0.06}$	−10.87	190.57/151
XMM8	55787	$1.63^{+0.05}_{-0.05}$	$1.34^{+0.02}_{-0.02}$	$1.41^{+0.05}_{-0.05}$	−10.85	179.59/163
XMM9	55800	$1.43^{+0.10}_{-0.10}$	$1.31^{+0.05}_{-0.05}$	$0.30^{+0.02}_{-0.02}$	−11.51	107.40/129
XMM10	55810	$1.58^{+0.08}_{-0.08}$	$1.39^{+0.04}_{-0.04}$	$0.58^{+0.03}_{-0.03}$	−11.26	154.57/145
XMM11	55824	$1.51^{+0.11}_{-0.12}$	$1.41^{+0.06}_{-0.06}$	$0.37^{+0.03}_{-0.03}$	−11.46	154.39/121
XMM12	55836	$1.51^{+0.08}_{-0.08}$	$1.34^{+0.04}_{-0.04}$	$0.78^{+0.04}_{-0.05}$	−11.10	167.89/144

variations with the stacked observations created using Swift data. During the first observation, referred to as XMM1, we found that the source spectrum had a spectral index of 1.69 ± 0.01 with a relatively lower hydrogen column density of $1.29 \pm 0.01 \times 10^{22}$ cm^{-2}. The `powerlaw` normalization and flux are found to be highest (see Table 3) in that particular observation. In the following observation, XMM2, the spectrum hardened with $\Gamma = 1.54 \pm 0.01$ and associated $N_{\rm H}$ increased to $1.42 \pm 0.02 \times 10^{22}$ cm^{-2}. The normalization and the flux were reduced substantially. Later, on MJD 55697, we fitted the XMM3 spectrum where Γ was found to be highest among all the XMM-Newton observations, having a value of 1.87 ± 0.05. The flux decreased dramatically to -11.14×10^{-11} from -10.15×10^{-11} erg cm^{-2} s^{-1}. This sudden dip in the flux could be associated with the dips found in the long-term light curve (V. Mangano et al. 2016; E. Seifina et al. 2017). During XMM4 observation, the source spectrum returned to a harder spectrum with $\Gamma = 1.55 \pm 0.02$.

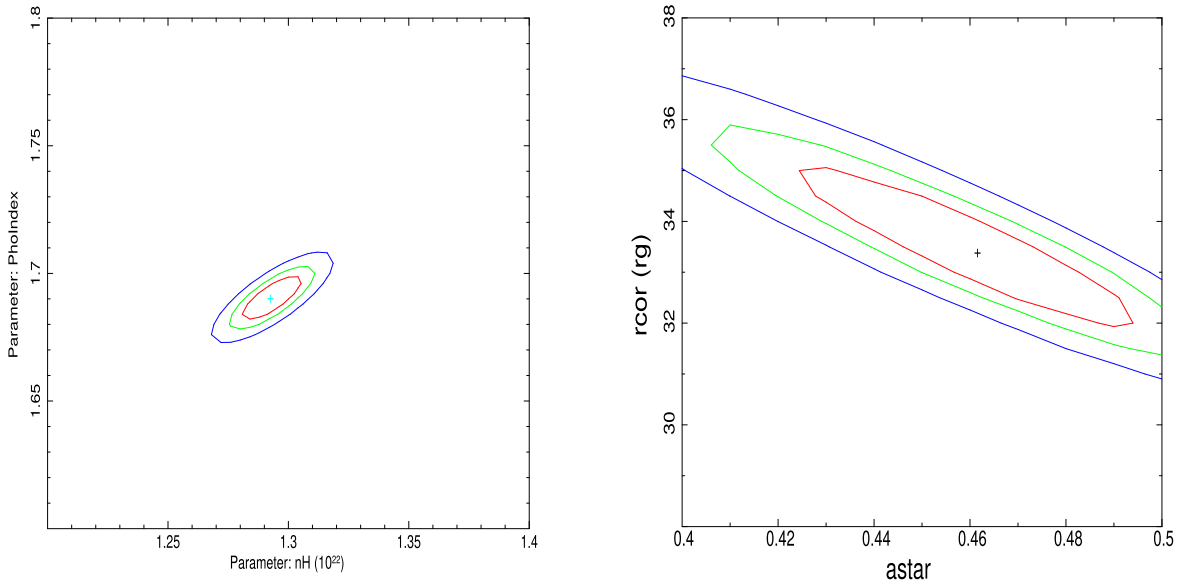

Figure 4. Contours of confidence are plotted for Swift/XRT observations fitted with the `powerlaw` and Optxagnf models.

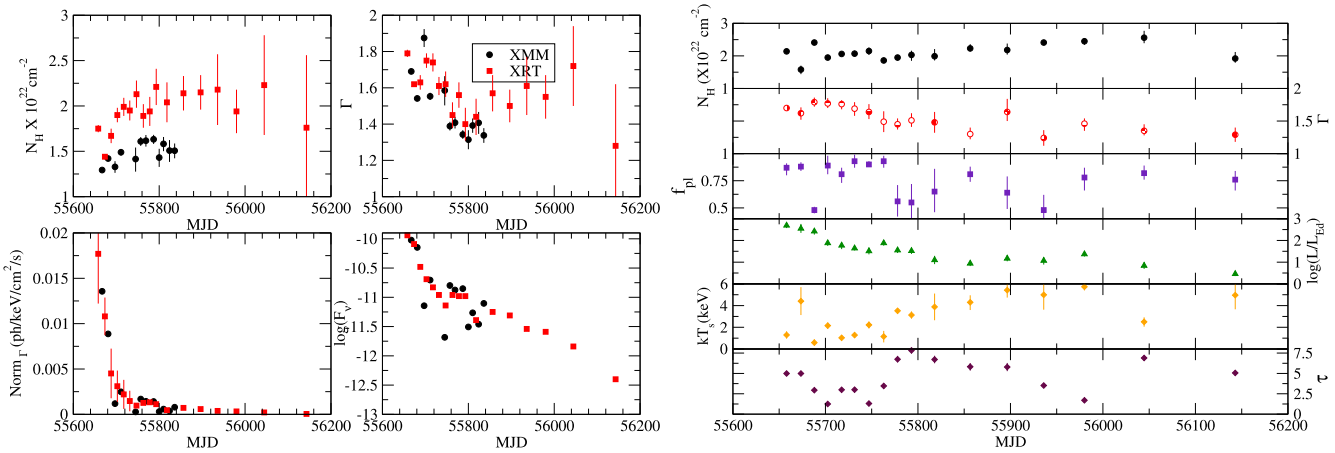

Figure 5. The variation in spectral parameters of Swift J1644+57 is presented for the `powerlaw` and `optxagnf` models. Only stacked Swift/XRT data are employed to fit the `optxagnf` model.

The concurrent flux increased from the previous observation. Later, in the XMM5 observation, we found an upward variation in the spectral index with $\Gamma = 1.59 \pm 0.08$. However, considering the error, the spectral index could be in a similar range as the XMM4 observation. The normalization and flux decreased rapidly, and the observed values are the lowest among all the XMM-Newton observations. Thereafter, both the flux and normalization increased with decreased spectral index. Post XMM5, the `powerlaw` fitted spectra exhibited a steady decrease in the flux with occasional variation in the spectral index. The source normalization also varied from 13.56×10^{-3} to 0.78×10^{-3} ph cm^{-2} s^{-1} throughout the XMM-Newton observations.

The results obtained from the baseline `powerlaw` model, presented in Table 3, suggest a good fit using a single power-law component. We found no residuals around the low-energy part, which could indicate the presence of a soft excess (K. A. Arnaud et al. 1985; K. P. Singh et al. 1985) or a thermal component from the disk, often visible for X-ray TDE (S. Gezari 2021). The Swift and XMM-Newton data within the overlapping time broadly exhibited similar spectral variation with increasing N_H associated with decreasing spectral index. The overall flux of Swift J1644+57 decreased. We found a lower and more confined variation in $N_{\rm H}$ from the XMM-Newton observations as compared to the Swift observations. However, the variation in $N_{\rm H}$ from the observations with both satellites remained similar throughout the entire period. We did not find the presence of the iron Kα line throughout the disruption event. The degrees of freedom for `powerlaw` fitting were higher for Swift observations compared to the XMM-Newton observations.

3.2.1. *Optxagnf*

The `Optxagnf` model, proposed by C. Done et al. (2012), provides an in-depth understanding of the spectral parameters as the parameters are generated from a physical picture of the accretion disk around the AGNs. The model-fitted parameters include the luminosity, coronal radius parameter ($R_{\rm cor}$), spin of the central black hole, soft-excess temperature, optical depth, spectral index, and the fraction of Comptonized photons. It should be noted that `Optxagnf` is the only publicly available

model to fit the X-ray spectra of AGNs where R_{cor} could be estimated. We employed this model to fit the XRT spectra. The model in xspec reads as TBabs□zTBabs□(optxagnf).

The model spectrum computes both soft-excess and Comptonized photons. The accretion rate governed by the mass of the central black hole determines the luminosity of the source (in units of Eddington luminosity—$\log(L/L_{Edd})$). The geometry of the Optxagnf model separates the accretion disk into three regions. First, the disk emission is produced through a color temperature-corrected blackbody emission from radii $R_{out} > r > R_{cor}$, where R_{out} and R_{cor} are the outer edge of the disk and the corona, respectively. Luminosity is computed keeping the distance and mass constant, while the mass-to-energy conversion efficiency factor (η) depends on the spin. Second, at $r < R_{cor}$, the emission is dominated by Comptonized emission from a warm and optically thick medium. The third region where inverse Comptonization occurs is the optically thin corona around the disk, and the fraction of inverse Comptonization can be estimated from the f_{pl} parameter during the spectral fitting. The temperature and optical depth of the warm, optically thick medium could be found from kT_s and τ, respectively. The model calculates the primary emission of Comptonized photons using the Nthcomp model, where the seed photon temperature is kept fixed at $r = R_{cor}$, and the electron temperature of the optically thin hot corona is frozen at 100 keV. We freeze the mass of the black hole at $3 \times 10^6 M_\odot$ (J. S. Bloom et al. 2011b). The Galactic N_H along the line of Swift J1644+57 remained frozen at 0.016×10^{22} cm^{-2} while performing the fitting. According to the model, it was suggested to keep the normalization frozen at unity. The redshift $z = 0.354$ and distance $d = 1402.8$ Mpc are also kept fixed (A. J. Levan et al. 2011). The $\log(r_{out})$ is kept fixed at 5 since the apogee of extremely elongated TDEs, capable of explaining lengthy disruption events (K. Hayasaki et al. 2013; L. Dai et al. 2015; K. Hayasaki et al. 2018), could reach up to $10^4-10^5\, r_g$. The remaining parameters are left free to vary. It should be noted that the reported luminosities in Table 4 are isotropic and model-dependent without employing the beaming corrections. From Table 3, we can see that the power-law model fits the spectra of Swift J1644+57 well, and the soft X-ray excess is absent in the spectra. Thus, we freeze the kT_s at 0.1 keV and τ at a maximum value of 5.0. Initially, we left the f_{pl} thawed. We observed that the f_{pl} values saturated in most cases. Later, better fits were obtained while fitting the spectra with variable kT_s and τ, and are presented in Table 4. We observed that the warm corona temperature and optical depth remained high across all observations except XRT3. We found that kT_s gradually increases as the event progresses and remains within $0.59 \leqslant kT_s \leqslant 5.73$. On the other hand, the variation in the optical depth remained nonmonotonic within the limit $1.25 \leqslant \tau \leqslant 7.83$. The variation in f_{pl} remained within the range of $0.48 \leqslant f_{pl} \leqslant 0.93$ during our observation period. For TDEs, this is expected and is conjectured by J. Chakraborty et al. (2026). Optxagnf fitted spectra for three epochs are presented in Figure 3, and the variation in fitted parameters with time is plotted in the right panel of Figure 5 and is presented in Table 4.

We fitted the 0.3–10 keV stacked Swift spectra for the entire episode of TDE. The spectra fitted alone with the Optxagnf model provided good statistics with $\chi^2_{red} \sim 1$. The model-fitted spectral parameters are presented in Table 4. We found the luminosity of the source exceeded nearly 500 times the Eddington luminosity during the initial few days of the event. This agrees with the earlier studies like B. A. Zauderer et al. (2013) and is also seen from the current fitting with Optxagnf model. Over time, the luminosity of the source decreased nearly 200 times from the initial phase, but never went into the sub-Eddington regime during the period of our observation. The variation in N_H remained similar to what has been observed during the fitting with the powerlaw model. The spin of the central black hole remained within the range of $0.4 < a^* < 0.8$, making it an intermediate spinning black hole. During the initial days, the coronal parameter of the source was observed at $31 \pm 2\, r_g$. The right panel of Figure 4 represents the confidence contours of spin (a) versus R_{cor}. The coronal radius parameter was found to vary within $31 < R_{cor} < 65\, r_g$. We only used the stacked Swift data for Optxagnf fitting as it provides better data quality to understand the long-timescale variations of Swift J1644+57 during its tidal disruption episode.

4. Discussion

We studied Swift J1644+57 during its TDE of 2011–2012 using Swift and XMM-Newton data within the energy range 0.3–10 keV. We employed the powerlaw as our phenomenological model and a physical model, such as Optxagnf, to understand the behavior of the source as the event progresses. Being a jetted TDE, the source exhibited variability in both the spectral and temporal domains and is one of the most studied TDEs to date. During our analysis, we found that there are several similarities between TDEs and the declining phase of an outbursting GBH. The similarities between GBH transients and TDEs are seen from their spectral energy distributions and the decaying luminosity with time. The X-ray spectral indices of GBHs are found to decrease in the luminosity decay phase (J. E. McClintock et al. 2009). Likewise, the decreasing tendency of the spectral index has also been observed in Swift J1644+57 (E. Seifina et al. 2017). Recent NICER observations (K. C. Gendreau et al. 2012) of MAXI J1820+070 provided evidence of a dynamically contracting corona for the onset stage of the flare (E. Kara et al. 2019). A. Jana et al. (2016) explained, using the two-component advective flow model (S. Chakrabarti & L. G. Titarchuk 1995), why the Compton cloud expanded at the declining phase of a low inclination GBH, MAXI J1836−194, during the 2011 outburst. The variation in the corona size is also observed for AGN IRAS 13224−3809 (W. N. Alston et al. 2020). Apart from R_{cor} variation, relativistic jet launching is another phenomenon that GBH transients and TDEs have in common (I. F. Mirabel & L. F. Rodríguez 1994; B. A. Zauderer et al. 2011; R. Blandford et al. 2019; D. Patra et al. 2019; M. Espinasse et al. 2020).

4.1. Nuclear Properties

X-ray emission from Swift J1644+57 has been observed for around 600 days. The hard X-ray component was found to dominate, and the radiation is conjectured to be beamed (B. A. Zauderer et al. 2013), and many authors. From our spectral analysis, we find that the source exhibited variations in hydrogen column density (N_H). Figure 5 represents the variation in powerlaw fitted parameters. We find that the hydrogen column density, at the beginning, was higher at

Table 4
`Optxagnf` Fitted Spectral Parameter Are Presented

ID	MJD (days)	$N_{\rm H}$ (10^{22} ecm^{-2})	$\log(\frac{L}{L_{Edd}})$	a^*	$R_{\rm cor}$ (r_g)	kT_s (keV)	τ	Γ	$f_{\rm pl}$	dof/chi^2
XRT1	55658	$2.14^{+0.06}_{-0.07}$	$2.69^{+0.13}_{-0.12}$	$0.62^{+0.03}_{-0.04}$	$31^{+2.1}_{-2.3}$	$1.29^{+0.34}_{-0.33}$	$4.99^{+0.23}_{-0.24}$	$1.70^{+0.04}_{-0.04}$	$0.87^{+0.04}_{-0.07}$	887/830
XRT2	55673.5	$1.58^{+0.12}_{-0.14}$	$2.55^{+0.21}_{-0.20}$	$0.58^{+0.11}_{-0.13}$	$31^{+3.3}_{-4.1}$	$4.41^{+1.29}_{-1.28}$	$4.99^{+0.31}_{-0.27}$	$1.62^{+0.09}_{-0.10}$	$0.88^{+0.04}_{-0.04}$	1058/938
XRT3	55688	$2.41^{+0.04}_{-0.03}$	$2.42^{+0.11}_{-0.15}$	$0.49^{+0.04}_{-0.06}$	$32^{+2.5}_{-2.2}$	$0.59^{+0.30}_{-0.25}$	$2.94^{+0.22}_{-0.22}$	$1.79^{+0.07}_{-0.07}$	$0.48^{+0.03}_{-0.03}$	722/689
XRT4	55702.5	$1.95^{+0.08}_{-0.07}$	$1.88^{+0.13}_{-0.13}$	$0.60^{+0.05}_{-0.04}$	$35^{+3.1}_{-3.6}$	$2.15^{+0.29}_{-0.26}$	$1.25^{+0.15}_{-0.15}$	$1.77^{+0.08}_{-0.07}$	$0.89^{+0.09}_{-0.08}$	625/703
XRT5	55717.5	$2.06^{+0.05}_{-0.05}$	$1.77^{+0.16}_{-0.17}$	$0.63^{+0.06}_{-0.06}$	$43^{+3.7}_{-3.4}$	$1.03^{+0.25}_{-0.22}$	$2.99^{+0.23}_{-0.25}$	$1.76^{+0.06}_{-0.08}$	$0.81^{+0.06}_{-0.08}$	575/646
XRT6	55731.5	$2.07^{+0.09}_{-0.08}$	$1.64^{+0.10}_{-0.10}$	$0.61^{+0.07}_{-0.06}$	$51^{+4.1}_{-4.3}$	$1.28^{+0.24}_{-0.26}$	$3.00^{+0.28}_{-0.28}$	$1.69^{+0.10}_{-0.11}$	$0.93^{+0.06}_{-0.06}$	683/638
XRT7	55747	$2.15^{+0.11}_{-0.12}$	$1.51^{+0.16}_{-0.15}$	$0.67^{+0.10}_{-0.10}$	$58^{+3.8}_{-4.1}$	$2.22^{+0.31}_{-0.32}$	$1.30^{+0.27}_{-0.27}$	$1.64^{+0.12}_{-0.11}$	$0.90^{+0.03}_{-0.02}$	593/587
XRT8	55763	$1.86^{+0.08}_{-0.06}$	$1.88^{+0.13}_{-0.12}$	$0.62^{+0.07}_{-0.08}$	$61^{+4.6}_{-4.1}$	$1.15^{+0.52}_{-0.54}$	$3.46^{+0.35}_{-0.36}$	$1.49^{+0.16}_{-0.16}$	$0.93^{+0.05}_{-0.06}$	550/594
XRT9	55778	$1.95^{+0.05}_{-0.09}$	$1.55^{+0.14}_{-0.13}$	$0.54^{+0.04}_{-0.04}$	$58^{+4.5}_{-4.5}$	$3.52^{+0.24}_{-0.24}$	$6.74^{+0.41}_{-0.38}$	$1.45^{+0.09}_{-0.08}$	$0.56^{+0.15}_{-0.14}$	510/547
XRT10	55793	$2.03^{+0.13}_{-0.18}$	$1.52^{+0.14}_{-0.14}$	$0.58^{+0.10}_{-0.10}$	$61^{+4.1}_{-4.2}$	$3.13^{+0.33}_{-0.33}$	$7.83^{+0.44}_{-0.39}$	$1.51^{+0.11}_{-0.10}$	$0.55^{+0.17}_{-0.17}$	511/527
XRT11	55818	$1.99^{+0.22}_{-0.13}$	$1.10^{+0.19}_{-0.19}$	$0.71^{+0.11}_{-0.15}$	$58^{+5.2}_{-5.1}$	$3.88^{+1.23}_{-1.23}$	$6.71^{+0.46}_{-0.46}$	$1.48^{+0.16}_{-0.16}$	$0.65^{+0.21}_{-0.19}$	426/463
XRT12	55856.5	$2.23^{+0.13}_{-0.09}$	$0.94^{+0.11}_{-0.12}$	$0.66^{+0.13}_{-0.09}$	$63^{+5.1}_{-5.2}$	$4.30^{+0.65}_{-0.71}$	$5.82^{+0.45}_{-0.47}$	$1.30^{+0.10}_{-0.08}$	$0.81^{+0.07}_{-0.07}$	444/461
XRT13	55896.5	$2.18^{+0.20}_{-0.14}$	$1.17^{+0.15}_{-0.13}$	$0.55^{+0.22}_{-0.16}$	$60^{+5.7}_{-6.1}$	$5.42^{+0.60}_{-0.68}$	$5.79^{+0.50}_{-0.51}$	$1.64^{+0.20}_{-0.14}$	$0.64^{+0.15}_{-0.15}$	440/508
XRT14	55936	$2.41^{+0.07}_{-0.07}$	$1.07^{+0.16}_{-0.18}$	$0.67^{+0.11}_{-0.12}$	$64^{+5.0}_{-3.4}$	$4.99^{+1.37}_{-1.37}$	$3.52^{+0.17}_{-0.17}$	$1.24^{+0.12}_{-0.12}$	$0.48^{+0.14}_{-0.13}$	246/300
XRT15	55980	$2.45^{+0.08}_{-0.11}$	$1.37^{+0.08}_{-0.11}$	$0.53^{+0.14}_{-0.10}$	$61^{+4.3}_{-4.6}$	$5.73^{+0.31}_{-0.33}$	$1.70^{+0.29}_{-0.31}$	$1.46^{+0.08}_{-0.11}$	$0.78^{+0.09}_{-0.09}$	329/368
XRT16	56044.5	$2.56^{+0.21}_{-0.17}$	$0.84^{+0.13}_{-0.15}$	$0.76^{+0.12}_{-0.10}$	$65^{+4.2}_{-3.8}$	$2.50^{+0.42}_{-0.44}$	$6.90^{+0.33}_{-0.33}$	$1.35^{+0.10}_{-0.07}$	$0.82^{+0.07}_{-0.06}$	166/192
XRT17	56143	$1.92^{+0.20}_{-0.13}$	$0.46^{+0.10}_{-0.10}$	$0.68^{+0.09}_{-0.08}$	$64^{+5.2}_{-4.9}$	$4.96^{+1.30}_{-1.30}$	$5.06^{+0.31}_{-0.32}$	$1.29^{+0.11}_{-0.11}$	$0.76^{+0.08}_{-0.10}$	99.5/100

Note. We used stacked Swift/XRT over XMM-Newton as the former provides more degrees of freedom over the latter. The following parameters are kept frozen while fitting: $N_{\rm H}^{\rm Gal} = 0.016 \times 10^{22}$ cm^{-2}, model normalization $N_{\rm optx} = 1$, redshift $z = 0.354$, distance $d = 1402.8$ Mpc, and $\log(r_{\rm out}) = 5$.

$1.75 \pm 0.04 \times 10^{22}$ cm^{-2}. Later, in XRT2, the $N_{\rm H}$ dropped to $1.44 \pm 0.04 \times 10^{22}$ cm^{-2}. Post XRT2, the spectra showed a gradual increase in the value of $N_{\rm H}$ and plateaued at a late stage. Similar observational findings are also seen through XMM-Newton spectra fitted with the `powerlaw` model and Swift spectra fitted with the `Optxagnf` model. The variation in $N_{\rm H}$ could be a generic property of the jetted TDEs.

E. Seifina et al. (2017) reported that the spectral index of individual spectra observed by Swift/XRT saturates after MJD 55730; i.e., after eighty days since the start of the event. We used stacked spectra of Swift/XRT where the spectral indices are observed to be decreasing up to MJD 55800. However, after that, the spectral indices increased. But, finally, at XRT17 observation, the spectral index was 1.28 ± 0.34. Both Swift and XMM-Newton data are employed to measure the spectral indices variation within MJD 55650 to MJD 55800, where a similar pattern has been found. Using the `Optxagnf` model, we have also observed similar variations. The increase in the X-ray spectral indices after 150 days could be associated with the increased optical activity after ∼30–50 days since the initial observations (A. J. Levan et al. 2016). We find that N_H and Γ are weakly anticorrelated with a Pearson correlation coefficient of −0.22, and the variation can be observed in Figure 6.

The `Optxagnf` model provides several parameters of the source. Among them, we find that the luminosity, in terms of $\log(L/L_{\rm Edd})$, is highly sensitive to the fitting. The fitted spectra exhibited a variation on the order of 2 within the range of our observations. During the initial days, Swift J1644+57 had a bolometric luminosity of around 500 times the Eddington limit. In the entire observation, the source luminosity was in the super-Eddington regime. The luminosity followed a steady decrease from the initial days, with occasional variation in between, which can be associated with the intrinsic photon count variation in the light curve. During XRT17, the last observation, the source luminosity decreased to nearly 3 times the Eddington limit. We find the source luminosity weakly anticorrelated with the hydrogen column density, with a Pearson correlation coefficient of −0.31, and is plotted in Figure 6(a).

The spin of Swift J1644+57, measured using the a^* parameter of the `Optxagnf` model, exhibited a region of an intermediate spinning black hole. We find a^* to vary from 0.4 to 0.8, as presented in Figure 6(f). The value of the spin aligns

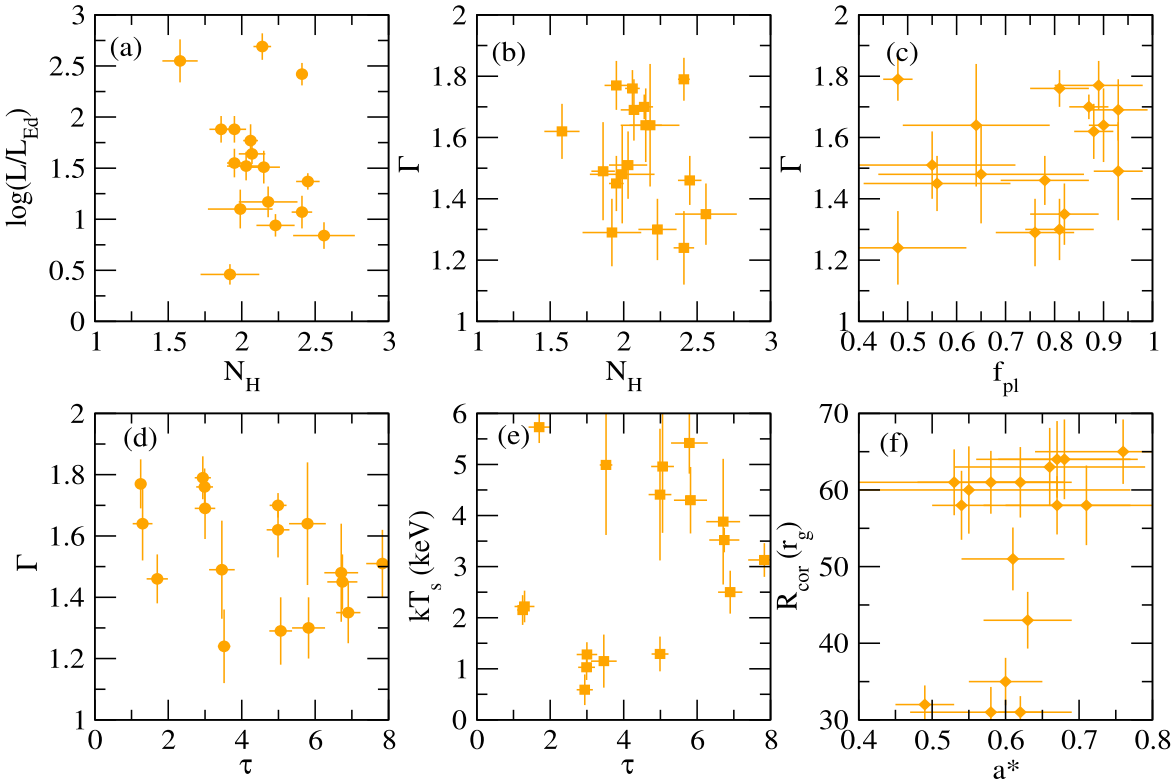

Figure 6. `Optxagnf` fitted spectral parameters variation with each other of Swift J1644+57 are presented. Panel (a) shows the variation in N_H with respect to the normalized luminosity. The variation in N_H with respect to Γ is shown in panel (b). Panel (c) demonstrates the weak correlation between Γ and scattering fraction $f_{\rm pl}$. Variation in Γ and τ can be observed in panel (d). Panel (e) presents the variation in $R_{\rm cor}$ and spin parameter. Uncorrelated variation between spin and $R_{\rm cor}$ can be observed in panel (e).

with the earlier claim by A. Tchekhovskoy et al. (2014), where they predicted the spin of the source should be greater than $\geqslant$0.5.

4.2. Coronal Variations

The hard X-ray photons, emerging from the vicinity of a black hole, are thought to originate from a corona which can be formed through magnetic reconnection in the accretion disk (A. A. Galeev et al. 1979; B. F. Liu et al. 2002). There are a few practical models of corona that have been proposed so far. The *lampost* model (A. Martocchia & G. Matt 1996; G. Miniutti & A. C. Fabian 2004) provides physical explanations of the X-ray spectra from the AGNs; C. Done et al. (2012) constructed the `Optxagnf` model, which computes the size of the corona, $R_{\rm cor}$, from the spectral fitting. It has also been observed that the nature of the corona is dynamic for GBHs (E. Kara et al. 2019) and for AGNs (W. N. Alston et al. 2020). That is why it is crucial to explore how the corona size evolves with time for TDEs.

To measure the $R_{\rm cor}$ variation of Swift J1644+57, we employ the `Optxagnf` model to determine the spectral fits using the stacked Swift/XRT data. Through our spectral fitting, we find that at the peak luminosity of Swift J1644+57, the radial size of the corona was $31 \pm 2.3\, r_{\rm g}$. Subsequently, an almost similar size of the $R_{\rm cor}$ was found in the XRT2 and XRT3 observational epochs. The size of the corona increases $35 \pm 3.6\, r_{\rm g}$ in the XRT4 epoch. Later on, in the XRT5 and XRT6 epochs, the $R_{\rm cor}$ keeps increasing to $43 \pm 3.7\, r_{\rm g}$ and $51 \pm 4.3\, r_{\rm g}$, respectively. During the XRT7 observation, the $R_{\rm cor}$ is $58 \pm 4.1\, r_{\rm g}$. Up to the XRT7 observation, we observed a sharp rise in the $R_{\rm cor}$. The fitted value of the $R_{\rm cor}$ is $61 \pm 4.2\, r_{\rm g}$ at XRT8 and drops to $58 \pm 4.5\, r_{\rm g}$ at XRT10. From the XRT10 to XRT17 observations, the $R_{\rm cor}$ varies little from $58\, r_{\rm g}$ to $64\, r_{\rm g}$, indicating a saturation level of the parameter. All estimated values of the coronal parameters are depicted in Figures 5 and 6. In addition, we find through our analysis that the $R_{\rm cor}$ is anticorrelated with the luminosity $\log(L/L_{\rm Edd})$ with the Pearson correlation coefficient: -0.87. The Markov Chain Monte Carlo plots showing the `Optxagnf` parameters for XRT2 and XRT15 are presented in Figure 7.

Recently, A. Mummery & S. A. Balbus (2021) proposed the disk–corona model to explain nonthermal hard X-ray emissions from X-ray TDEs. According to their prescription, the size of the corona would depend on the disk luminosity as follows:

$$R_{\rm cor} = \begin{cases} R_I, & \text{initial size of corona,} \\ R_I + (R_C - R_I) f(l), & \text{intermediate size of corona,} \\ R_C, & \text{final size of corona,} \end{cases} \tag{8}$$

where

$$f(l) = \frac{l_I - l(t)}{l_I - l_C},$$

and l_I, l_C, and $l(t)$ are the initial, final, and time-dependent Eddington ratios, respectively. Starting with an initial $R_{\rm cor}$ R_I, the corona expands following the decay pattern of the luminosity profile and finally saturates to a value of R_C. We adopt $R_I = 30\, r_{\rm g}$ and $R_C = 65\, r_{\rm g}$. The normalized disk

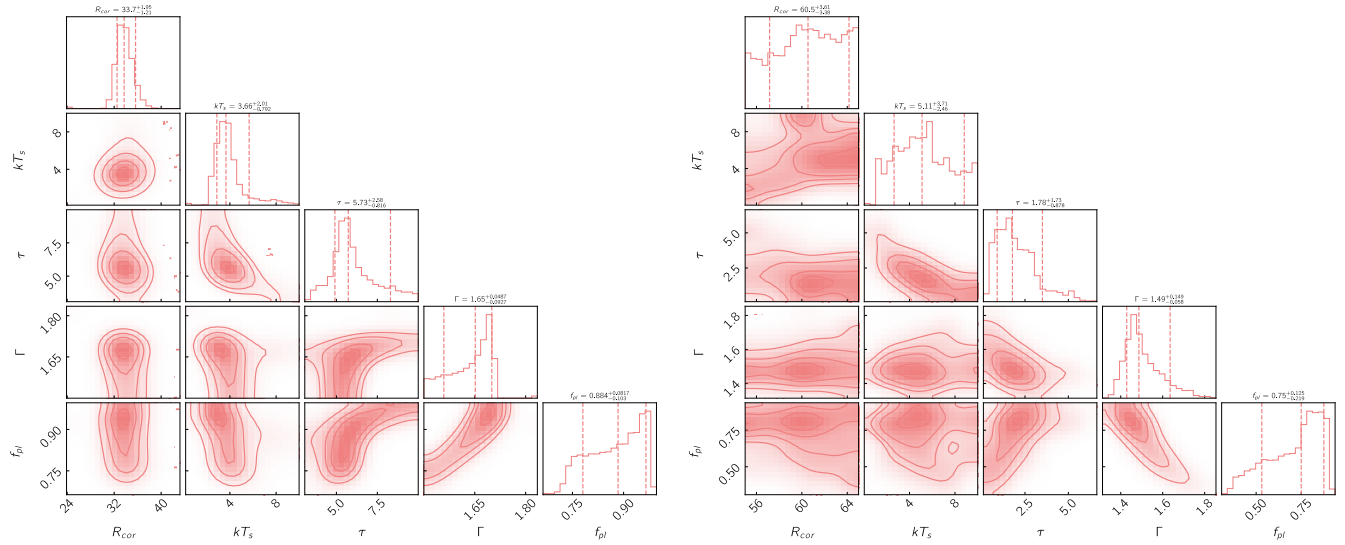

Figure 7. Markov Chain Monte Carlo plots for parameter variations of XRT2 and XRT15 are presented. Goodman–Weare (EMCEE; D. Foreman-Mackey et al. 2013) is opted for 32 walkers and a chain length of 1 million iterations, where the transient phase is removed by burning the chain up to 9984 iterations. The spin parameter was kept frozen at $a^* = 0.60$ to perform the MCMCs.

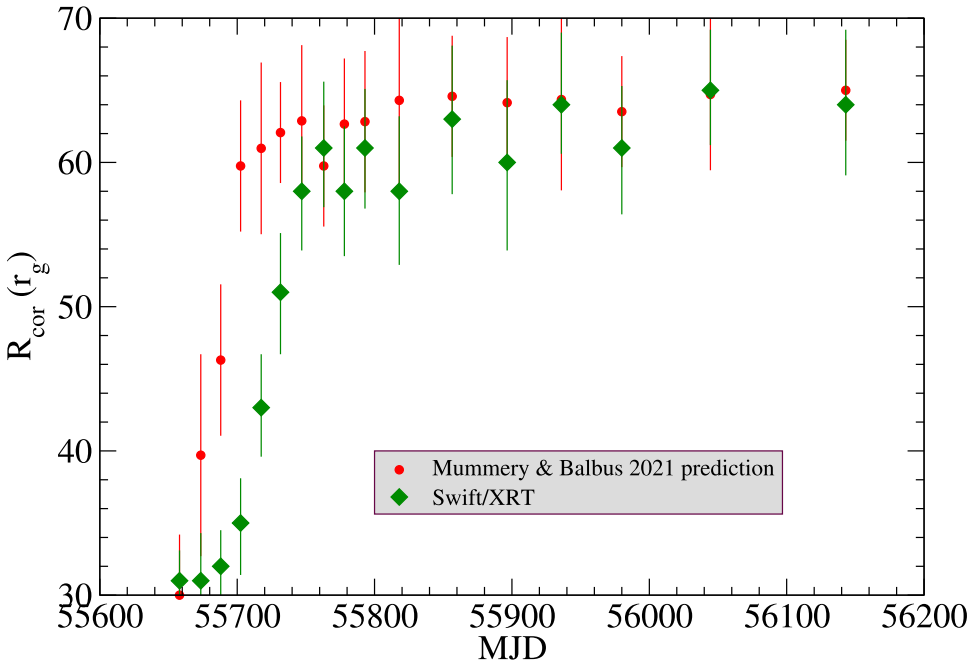

Figure 8. Coronal variation with time is presented for Swift J1644+57. Swift/XRT fitted values are presented by green diamond points. The red circles denote the theoretical values of R_{cor} as predicted by A. Mummery & S. A. Balbus (2021).

luminosity, $\log(L/L_{Edd})$, at each observational epoch is displayed in Table 4. The predicted R_{cor} at each epoch using Equation (8) is denoted with red circles in Figure 8. The error in the theoretical values is a contribution arising from the observational error in the measurement of luminosity as presented in Table 4. We find that the evolution of theoretically speculated corona size agrees with that of the observational R_{cor} parameter in Swift J1644+57, and considering the error bars, their variation remains similar.

Figure 9 gives a schematic view of the disk–corona–jet system for the early and late stages of Swift J1644+57. The physical scale of the disk and corona fits within the range of $2R_t \sim 100\, r_g$ for a $10^6\, M_\odot$ SMBH, where R_t is given by Equation (1). We presume that, in the initial days, the accretion rate was at the super-Eddington rate, and the corona was small. As the days progressed, the accretion rate reduced, and the magnetic flux became stronger, as suggested by A. Tchekhovskoy et al. (2014). This allows the disk to have a bigger corona than that of the initial state. Although the disk is yet in the super-Eddington regime at this moment, the bigger corona is likely to produce a larger number of high-energy X-ray photons via inverse Compton scattering. Within the first hundred days, the jet flux increases monotonically and is anticorrelated with the X-ray flux (E. Berger et al. 2012; E. Seifina et al. 2017), suggesting that the jet region also expands during this period. Depending on the quality and amount of the X-ray observational data, one can measure the coronal variation of the other three jetted TDEs and nonjetted

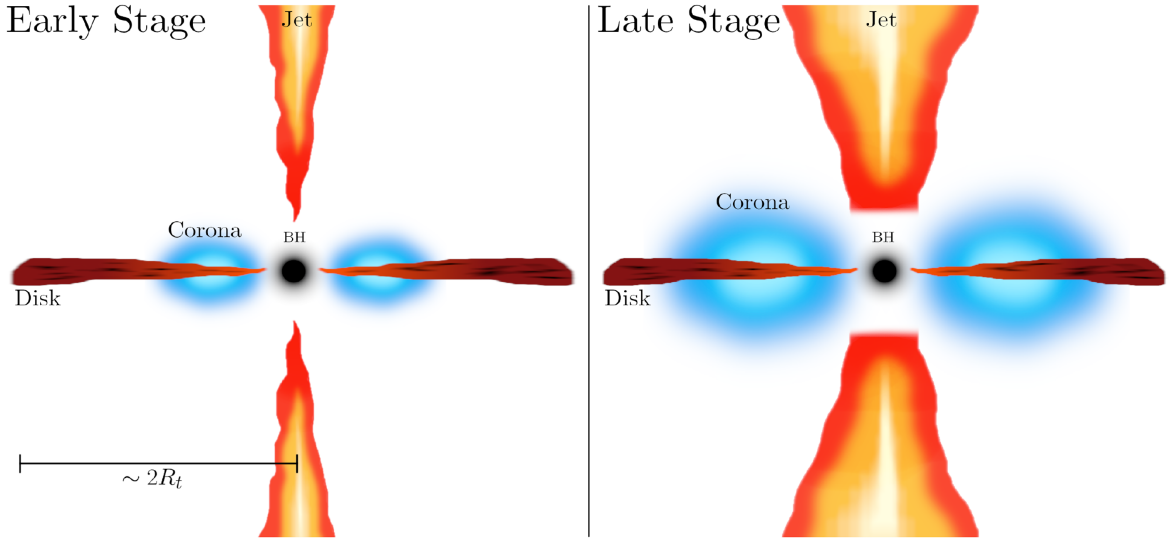

Figure 9. Edge-on view schematic diagram of $R_{\rm cor}$ variation in the early and late stages of Swift J1644+57. The system comprises a disk around the SMBH, a corona on the disk, and a jet. The disk size is twice the tidal disruption radii, which is approximately estimated to be $2R_{\rm t} \sim 100\ r_{\rm g}$ for the $10^6 M_\odot$ SMBH and a solar-type star (see 1).

TDEs using the same analysis as ours. This is also useful for improving the theoretical corona model in TDEs. More recently, J. Chakraborty et al. (2026) argued that the accretion disk of X-ray bright TDEs could be composed of a variable corona having lower electron temperature and higher optical depth, and can also be observed from the variation in the parameters presented in Table 4.

4.2.1. Viability of TDE Corona Models

It should be noted that, to date, there exists no publicly available model in XSPEC to fit the hyper accretion regime of Swift J1644+57. The source was one of the very few jetted TDEs ever observed with a QPO feature. The initial accretion rate was $\sim$1000 $L_{\rm Edd}$ and was widely explored for its unique attributes. While choosing the model, one must be extremely cautious. `Optxagnf` is the only model in XSPEC that applies to the super-Eddington accretion regime of the AGNs, and measures the coronal radius parameter.

According to the `Optxagnf` model (C. Done et al. 2012), in the $r \leqslant r_{\rm cor}$ region, the disk and the corona could coexist to make a "disk–corona" structure (A. A. Galeev et al. 1979; F. Haardt & L. Maraschi 1991; A. Martocchia & G. Matt 1996; B. F. Liu et al. 2002), and such a configuration also provides higher photon interception to the corona. The transition radius after which the radiation transfers from pure color-corrected blackbody to the inverse Comptonizations in the high τ and low kT_s and/or low τ and high kT_s regions is called the coronal radius. In reality, Compton up or down scattering in the radiation pressure supported torus is complex in nature (T. Kawaguchi 2003) due to the interplay between twisted magnetic field lines (Y.-F. Jiang et al. 2019) and the velocity field of electrons (A. Chatterjee et al. 2018). The Compton y-parameter is inadequate for interpreting Comptonized spectra in super-Eddington, jet-dominated accretion flows, as it assumes a thermal, homogeneous, isotropic electron plasma in the Thomson regime. In high-τ, advective, or nonthermal environments such as Swift J1644+57, y could become degenerate and physically misleading. Nevertheless, X-ray emission originated from the "disk–corona," or the corona as earlier suggested by W.-H. Lei et al. (2016), E. Kara et al. (2016), and V. Mangano et al. (2016). Moreover, the source exhibits Comptonized X-ray spectra with variable hardness that are well described by evolving Comptonization components, independent of the precise inner accretion flow geometry (J. S. Bloom et al. 2011a; D. N. Burrows et al. 2011).

Recently, J. Chakraborty et al. (2026) have proposed a coronal emission for TDEs (see their Figure 7) where the optical depth could be higher, accompanied by a lower electron temperature. The parameters obtained from the `Optxagnf` model, presented in Table 4, exhibit a similar nature of corona. Although the morphology of the TDE corona could depart from the structure of the warm corona, the thermal properties, such as high τ and kT_s, resemble the warm corona of the `Optxagnf` model. The variation in $R_{\rm cor}$ could be observed from the MCMC plots presented in Figure 7. However, it should be noted that `Optxagnf`, developed for AGNs, may not be physically self-consistent for hyper-Eddington jetted TDEs, such as for Swift J1644+57.

The high optical depth (τ) and low (kT_s) corona could form in the case of radiation pressure supported tori or super-Eddington thick disks, which were investigated by M. Abramowicz et al. (1978), M. Kozlowski et al. (1978), M. A. Abramowicz et al. (1980), B. Paczyński & P. J. Wiita (1980), M. Sikora (1981), J. Fukue (1982), S. K. Chakrabarti (1985a), P. Madau (1988), A. Ulmer (1997), Y.-F. Jiang et al. (2019), and Y.-F. Jiang & L. Dai (2024). Thick disks are capable of launching collimated jets (M. J. Rees et al. 1982; S. K. Chakrabarti 1985b) and could also produce QPOs through oscillations (M. Jaroszynski 1986). The radiative properties of the TDEs need to be explored in this regime. However, there are no models in XSPEC with the thick disk feature. Furthermore, under the ideal situation, one could be exploring the magnetically arrested disks (R. Narayan et al. 2003; A. Tchekhovskoy et al. 2014) to fit the broadband spectral energy distributions of the jetted TDEs. In future work, we will incorporate a simplified thick disk model in `XSPEC` to examine the parameters for several X-ray bright TDEs.

5. Summary

We have revisited the X-ray emission of the jetted TDE Swift J1644+57 between 2011 and 2012 by analyzing the archival Swift and XMM-Newton data with HEAsoft. Swift J1644+57 showed a massive TDE during 2011 and 2012, where the flux of the hard (3–10 keV) photons dominated that of the soft (0.2–2 keV) photons over the entire period. We have hypothesized that those hard photons originate from the Compton cloud, i.e., the corona, and have estimated the size of the corona by measuring the size of the hard X-ray emitted region using the publicly available model `Optxagnf`. Our key findings are summarized as follows.

1. We find that the spectral index nonmonotonically decreases with time, demonstrating that the fraction of harder photons increases with time. This indicates that the size of the Compton cloud gets larger because the soft photons are more scattered to be exhausted. We observed that the optical depth (τ) and the temperature of the warm corona (kT_s) remained high—a result that aligns with the J. Chakraborty et al. (2026) study.
2. By interpreting the hard X-ray-emitted region as a corona, we have estimated the size of the corona as a function of time. Considering the `Optxagnf` model, we confirm that the coronal radius parameter $R_{\rm cor}$ increases over time for the observed period. We also find that the evolution of the corona size agrees with the theoretical conjecture made by A. Mummery & S. A. Balbus (2021).
3. We find that the flux of hard and soft photons is highly correlated with the correlation coefficient $\rho_{\rm max} = 0.95$ throughout the event. Their correlation pattern has peaked at a zero delay. Moreover, the flux variabilities of the soft (0.2–2 keV) and hard (3–10 keV) photons correlate with each other with a Pearson correlation coefficient of 0.96. These correlations suggest that the soft and hard band photons are emitted from the same source.

Four jetted TDEs have been observed so far (S. B. Cenko et al. 2012; G. C. Brown et al. 2015; I. Andreoni et al. 2022). In the future, more exotic events could be observed by XRISM (M. Tashiro et al. 2018). The large field of view and imaging capability of the proposed-to-NASA mission AXIS (R. Mushotzky & AXIS Team 2019; C. S. Reynolds et al. 2023; S. Safi-Harb et al. 2023; M. Koss et al. 2025) could provide a detailed structure of the X-ray emitting region of these sources. Also, to perform the short-term timing studies and search for more QPOs among the AGNs, the large effective area and high throughput of the proposed-to-CSA Colibrì (I. Caiazzo et al. 2019; J. Heyl et al. 2019) and proposed-to-ESA NewAthena (M. Cruise et al. 2025) missions will be required in the future. Future proposed X-ray interferometric missions (W. Cash et al. 2000; W. Cash 2003; K. C. Gendreau et al. 2004; A. Chatterjee et al. 2017, 2018; A. Chatterjee 2018; P. Uttley et al. 2020; P. Gandhi 2024; K. A. Weaver et al. 2026) are essential to visualize the coronal variation in the configuration space, much like what the Event Horizon Telescope (Event Horizon Telescope Collaboration et al. 2025) has obtained in the radio and submillimeter range.

Acknowledgments

The authors acknowledge an anonymous reviewer for the constructive comments. A.C. acknowledges the UPES Seed grant (UPES/R&D/SoAE/25062025/23) for partially supporting this research. The research of A.C., S.H., and S.S. H. was supported by the Canadian Space Agency (CSA) and the Natural Sciences and Engineering Research Council of Canada (NSERC) through the Discovery Grants and the Canada Research Chairs programs. The Basic Science Research Program has supported K.H. through the National Research Foundation of Korea (NRF), funded by the Ministry of Education (2016R1A5A1013277 (K.H. and A.C.), 2020R1A2C1007219, and RS-2025-23323627 (K.H.)). K.H. thanks Andrew Mummery for fruitful discussions. A.J. acknowledges support from the Fondecyt fellowship (Proyecto 3230303). N.K. acknowledges funds from European Union—Next Generation EU, Mission 4 Component 1 CUP C53D23001330006 and INAF Large Grant 2023 BLOSSOM F.O. 1.05.23.01.13. Research work at the Physical Research Laboratory, Ahmedabad, is funded by the Department of Space, Government of India. This research has made use of data and/or software provided by the High Energy Astrophysics Science Archive Research Center (HEASARC), which is a service of the Astrophysics Science Division at NASA/GSFC and the High Energy Astrophysics Division of the Smithsonian Astrophysical Observatory. This research has made use of the NASA/IPAC Extragalactic Database (NED), which is operated by the Jet Propulsion Laboratory, California Institute of Technology, under contract with the National Aeronautics and Space Administration. This research has made use of the SIMBAD database, operated at CDS, Strasbourg, France.

ORCID iDs

Arka Chatterjee https://orcid.org/0000-0003-3932-6705
Kimitake Hayasaki https://orcid.org/0000-0003-4799-1895
Prantik Nandi https://orcid.org/0000-0003-3840-0571
Neeraj Kumari https://orcid.org/0000-0003-0071-8947
Skye R. Heiland https://orcid.org/0000-0001-5294-7667
Arghajit Jana https://orcid.org/0000-0001-7500-5752
Sachindra Naik https://orcid.org/0000-0003-2865-4666
Samar Safi-Harb https://orcid.org/0000-0001-6189-7665

References

Abramowicz, M., Jaroszynski, M., & Sikora, M. 1978, A&A, 63, 221
Abramowicz, M. A., Calvani, M., & Nobili, L. 1980, ApJ, 242, 772
Alexander, K. D., van Velzen, S., Horesh, A., & Zauderer, B. A. 2020, SSRv, 216, 81
Alexander, T. 1997, ASSL, 218, 163
Alston, W. N., Fabian, A. C., Kara, E., et al. 2020, NatAs, 4, 597
Alston, W. N., Parker, M. L., Markevičiūtė, J., et al. 2015, MNRAS, 449, 467
Andreoni, I., Coughlin, M. W., Perley, D. A., et al. 2022, Natur, 612, 430
Arnaud, K. A. 1996, ASPC, 101, 17
Arnaud, K. A., Branduardi-Raymont, G., Culhane, J. L., et al. 1985, MNRAS, 217, 105
Ashton, D. I., & Middleton, M. J. 2021, MNRAS, 501, 5478
Bade, N., Komossa, S., & Dahlem, M. 1996, A&A, 309, L35
Bennett, C. L., Halpern, M., Hinshaw, G., et al. 2003, ApJS, 148, 1
Berger, E., Zauderer, A., Pooley, G. G., et al. 2012, ApJ, 748, 36
Blandford, R., Meier, D., & Readhead, A. 2019, ARA&A, 57, 467
Bloom, J. S., Butler, N. R., Cenko, S. B., & Perley, D. A. 2011a, GCN, 11847, 1
Bloom, J. S., Giannios, D., Metzger, B. D., et al. 2011b, Sci, 333, 203
Brown, G. C., Levan, A. J., Stanway, E. R., et al. 2015, MNRAS, 452, 4297

Burrows, D. N., Hill, J. E., Nousek, J. A., et al. 2005, SSRv, 120, 165
Burrows, D. N., Kennea, J. A., Ghisellini, G., et al. 2011, Natur, 476, 421
Caiazzo, I., Belloni, T., Cackett, E., et al. 2019, Unveiling the secrets of black holes and neutron stars with high-throughput, high-energy resolution X-ray spectroscopy, v1, Zenodo, doi:10.5281/zenodo.3824441
Cash, W. 2003, ExA, 16, 91
Cash, W., Shipley, A., Osterman, S., & Joy, M. 2000, Natur, 407, 160
Cendes, Y., Alexander, K. D., Berger, E., et al. 2021, ApJ, 919, 127
Cendes, Y., Wijers, R. A. M. J., Swinbank, J. D., et al. 2014, arXiv:1412.3986
Cenko, S. B., Krimm, H. A., Horesh, A., et al. 2012, ApJ, 753, 77
Chakrabarti, S., & Titarchuk, L. G. 1995, ApJ, 455, 623
Chakrabarti, S. K. 1985a, ApJ, 288, 1
Chakrabarti, S. K. 1985b, ApJ, 288, 7
Chakraborty, J., Masterson, M., Mummery, A., et al. 2026, ApJ, 1000, 95
Chatterjee, A. 2018, in Astrophysics and Space Science Proc., Vol. 53, Exploring the Universe: From Near Space to Extra-Galactic, ed. B. Mukhopadhyay & S. Sasmal (Springer), 29
Chatterjee, A., Chakrabarti, S. K., & Ghosh, H. 2017, MNRAS, 465, 3902
Chatterjee, A., Chakrabarti, S. K., Ghosh, H., & Garain, S. K. 2018, MNRAS, 478, 3356
Chatterjee, A., Dutta, B. G., Nandi, P., & Chakrabarti, S. K. 2020, MNRAS, 497, 4222
Cruise, M., Guainazzi, M., Aird, J., et al. 2025, NatAs, 9, 36
Dai, L., McKinney, J. C., & Miller, M. C. 2015, ApJApJL, 812, L39
De Colle, F., & Lu, W. 2020, NewAR, 89, 101538
Done, C., Davis, S. W., Jin, C., Blaes, O., & Ward, M. 2012, MNRAS, 420, 1848
Donley, J. L., Brandt, W. N., Eracleous, M., & Boller, T. 2002, AJ, 124, 1308
Edelson, R., Griffiths, G., Markowitz, A., et al. 2001, ApJ, 554, 274
Edelson, R., & Malkan, M. 2012, ApJ, 751, 52
Edelson, R., Turner, T. J., Pounds, K., et al. 2002, ApJ, 568, 610
Edelson, R. A., Alexander, T., Crenshaw, D. M., et al. 1996, ApJ, 470, 364
Eracleous, M., Livio, M., Halpern, J. P., & Storchi-Bergmann, T. 1995, ApJ, 438, 610
Espinasse, M., Corbel, S., Kaaret, P., et al. 2020, ApJL, 895, L31
Evans, P. A., Beardmore, A. P., Page, K. L., et al. 2009, MNRAS, 397, 1177
Event Horizon Telescope Collaboration, Akiyama, K., Albentosa-Ruíz, E., et al. 2025, A&A, 704, A91
Fabian, A. C., & George, I. M. 1991, LNP, 385, 169
Foreman-Mackey, D., Hogg, D. W., Lang, D., & Goodman, J. 2013, PASP, 125, 306
Fukue, J. 1982, PASJ, 34, 163
Galeev, A. A., Rosner, R., & Vaiana, G. S. 1979, ApJ, 229, 318
Gandhi, P. 2024, RSPTA, 382, 20230080
Gendreau, K. C., Arzoumanian, Z., & Okajima, T. 2012, SPIE, 8443, 844313
Gendreau, K. C., Cash, W. C., Shipley, A. F., & White, N. E. 2004, SPIE, 5168, 420
Gezari, S. 2021, ARA&A, 59, 21
Gierliński, M., Middleton, M., Ward, M., & Done, C. 2008, Natur, 455, 369
Gliozzi, M., Sambruna, R. M., Jung, I., et al. 2006, ApJ, 646, 61
González-Rodríguez, A., Castro-Tirado, A. J., Guerrero, M. A., & Castellón, A. 2014, RMxAC, 45, 73
Guillochon, J., & Ramirez-Ruiz, E. 2013, ApJ, 767, 25
Haardt, F., & Maraschi, L. 1991, ApJL, 380, L51
Hayasaki, K. 2021, NatAs, 5, 436
Hayasaki, K., Stone, N., & Loeb, A. 2013, MNRAS, 434, 909
Hayasaki, K., Stone, N., & Loeb, A. 2016, MNRAS, 461, 3760
Hayasaki, K., Zhong, S., Li, S., Berczik, P., & Spurzem, R. 2018, ApJ, 855, 129
Heyl, J., Caiazzo, I., Hoffman, K., et al. 2019, BAAS, 51, 175
Jana, A. 2022, MNRAS, 517, 3588
Jana, A., Debnath, D., Chakrabarti, S. K., Mondal, S., & Molla, A. A. 2016, ApJ, 819, 107
Jana, A., Kumari, N., Nandi, P., et al. 2021, MNRAS, 507, 687
Jana, A., Ricci, C., Tortosa, A., et al. 2026, A&A, 707, A213
Jaroszynski, M. 1986, MNRAS, 220, 869
Jiang, Y.-F., & Dai, L. 2024, arXiv:2408.16856
Jiang, Y.-F., Stone, J. M., & Davis, S. W. 2019, ApJ, 880, 67
Kara, E., Miller, J. M., Reynolds, C., & Dai, L. 2016, Natur, 535, 388
Kara, E., Steiner, J. F., Fabian, A. C., et al. 2019, Natur, 565, 198
Kawaguchi, T. 2003, ApJ, 593, 69
Komossa, S. 2017, AN, 338, 256
Kormendy, J., & Ho, L. C. 2013, ARA&A, 51, 511
Kormendy, J., & Richstone, D. 1995, ARA&A, 33, 581
Koss, M., Aftab, N., Allen, S. W., et al. 2025, arXiv:2511.00253
Kozlowski, M., Jaroszynski, M., & Abramowicz, M. A. 1978, A&A, 63, 209
Krawczynski, H., Hughes, S. B., Horan, D., et al. 2004, ApJ, 601, 151
Lei, W.-H., Yuan, Q., Zhang, B., & Wang, D. 2016, ApJ, 816, 20
Levan, A. J., Tanvir, N. R., Brown, G. C., et al. 2016, ApJ, 819, 51
Levan, A. J., Tanvir, N. R., Cenko, S. B., et al. 2011, Sci, 333, 199
Lin, D., Irwin, J. A., Godet, O., Webb, N. A., & Barret, D. 2013, ApJL, 776, L10
Liu, B. F., Mineshige, S., & Shibata, K. 2002, ApJL, 572, L173
Lodato, G., & Rossi, E. M. 2011, MNRAS, 410, 359
Madau, P. 1988, ApJ, 327, 116
Magorrian, J., & Tremaine, S. 1999, MNRAS, 309, 447
Mangano, V., Burrows, D. N., Sbarufatti, B., & Cannizzo, J. K. 2016, ApJ, 817, 103
Martocchia, A., & Matt, G. 1996, MNRAS, 282, L53
McClintock, J. E., Remillard, R. A., Rupen, M. P., et al. 2009, ApJ, 698, 1398
Merloni, A., Predehl, P., Becker, W., et al. 2012, arXiv:1209.3114
Merloni, A., Dwelly, T., Salvato, M., et al. 2015, MNRAS, 452, 69
Miniutti, G., & Fabian, A. C. 2004, MNRAS, 349, 1435
Mirabel, I. F., & Rodríguez, L. F. 1994, Natur, 371, 46
Mummery, A., & Balbus, S. A. 2021, MNRAS, 504, 4730
Mushotzky, R. & AXIS Team 2019, in LPI Contributions, Vol. 2135, The Space Astrophysics Landscape for the 2020s and Beyond, ed. J. E. Moores et al., 5025
Nandra, K., George, I. M., Mushotzky, R. F., Turner, T. J., & Yaqoob, T. 1997, ApJ, 476, 70
Narayan, R., Igumenshchev, I. V., & Abramowicz, M. A. 2003, PASJ, 55, L69
Nikołajuk, M., & Walter, R. 2013, A&A, 552, A75
Paczyński, B., & Wiita, P. J. 1980, A&A, 88, 23
Pandey, A., Gupta, A. C., & Wiita, P. J. 2017, ApJ, 841, 123
Park, G., & Hayasaki, K. 2020, ApJ, 900, 3
Pasham, D. R., Remillard, R. A., Fragile, P. C., et al. 2019, Sci, 363, 531
Patra, D., Chatterjee, A., Dutta, B. G., Chakrabarti, S. K., & Nandi, P. 2019, ApJ, 886, 137
Peterson, B. M., Ferrarese, L., Gilbert, K. M., et al. 2004, ApJ, 613, 682
Rees, M. J. 1988, Natur, 333, 523
Rees, M. J., Begelman, M. C., Blandford, R. D., & Phinney, E. S. 1982, Natur, 295, 17
Reis, R. C., Miller, J. M., Reynolds, M. T., et al. 2012, Sci, 337, 949
Reynolds, C. S., Kara, E. A., Mushotzky, R. F., et al. 2023, SPIE, 12678, 126781E
Ricci, C., Kara, E., Loewenstein, M., et al. 2020, ApJL, 898, L1
Ricci, C., Loewenstein, M., Kara, E., et al. 2021, ApJS, 255, 7
Rossi, E. M., Stone, N. C., Law-Smith, J. A. P., et al. 2021, SSRv, 217, 40
Safi-Harb, S., Burdge, K. B., Bodaghee, A., et al. 2023, arXiv:2311.07673
Saxton, C. J., Soria, R., Wu, K., & Kuin, N. P. M. 2012, MNRAS, 422, 1625
Seifina, E., Titarchuk, L., & Virgilli, E. 2017, A&A, 607, A38
Sikora, M. 1981, MNRAS, 196, 257
Singh, K. P., Garmire, G. P., & Nousek, J. 1985, ApJ, 297, 633
Stein, R., Velzen, S., Kowalski, M., et al. 2021, NatAs, 5, 510
Sun, H., Zhang, B., & Li, Z. 2015, ApJ, 812, 33
Tanaka, Y., Nandra, K., Fabian, A. C., et al. 1995, Natur, 375, 659
Tashiro, M., Maejima, H., Toda, K., et al. 2018, SPIE, 10699, 1069922
Tchekhovskoy, A., Metzger, B. D., Giannios, D., & Kelley, L. Z. 2014, MNRAS, 437, 2744
Ulmer, A. 1997, arXiv:astro-ph/9708265
Uttley, P., den Hartog, R., Bambi, C., et al. 2020, SPIE, 11444, 114441E
Vaughan, S., Edelson, R., Warwick, R. S., & Uttley, P. 2003, MNRAS, 345, 1271
Vaughan, S., & Uttley, P. 2005, MNRAS, 362, 235
Vaughan, S., & Uttley, P. 2006, AdSpR, 38, 1405
Walter, R., Bordas, P., Bozzo, E., et al. 2011, ATel, 3108, 1
Wang, J., & Merritt, D. 2004, ApJ, 600, 149
Weaver, K. A., Cann, J. M., Pfeifle, R., et al. 2026, arXiv:2601.20823
Wiersema, K., van der Horst, A. J., Levan, A. J., et al. 2012, MNRAS, 421, 1942
Yang, Q.-X., Xie, F.-G., Yuan, F., et al. 2015, MNRAS, 447, 1692
Zauderer, B. A., Berger, E., Margutti, R., et al. 2013, ApJ, 767, 152
Zauderer, B. A., Berger, E., Soderberg, A. M., et al. 2011, Natur, 476, 425
Zhang, Y. H., Treves, A., Maraschi, L., Bai, J. M., & Liu, F. K. 2006, ApJ, 637, 699
Zhong, S., Hayasaki, K., Li, S., Berczik, P., & Spurzem, R. 2023, ApJ, 959, 19